# Bayesian reconstruction of binary media with unresolved fine-scale spatial structures

J. Ray[a,*], S. A. McKenna[b], B. van Bloemen Waanders[c], Y. M. Marzouk[d]

[a]*MS 9159, PO Box 969, Sandia National Laboratories, Livermore, CA 94550-0969*
[b]*MS 0751, PO Box 5800, Sandia National Laboratories, Albuquerque, NM 87185-0751*
[c]*MS 1318, PO Box 5800, Sandia National Laboratories, Albuquerque, NM 87185-1318*
[d]*Massachusetts Institute of Technology, Cambridge, MA 02139*

**Abstract**

We present a Bayesian technique to estimate the fine-scale properties of a binary medium from multiscale observations. The binary medium of interest consists of spatially varying proportions of low and high permeability material with an isotropic structure. Inclusions of one material within the other are far smaller than the domain sizes of interest, and thus are never explicitly resolved. We consider the problem of estimating the spatial distribution of the inclusion proportion, $\mathbf{F}(\mathbf{x})$, and a characteristic length-scale of the inclusions, $\delta$, from sparse multiscale measurements. The observations consist of coarse-scale (of the order of the domain size) measurements of the effective permeability of the medium (i.e., static data) and tracer breakthrough times (i.e., dynamic data), which interrogate the fine scale, at a sparsely distributed set of locations. This ill-posed problem is regularized by specifying a Gaussian process model for the unknown field $\mathbf{F}(\mathbf{x})$ and expressing it as a superposition of Karhunen-Loève modes. The effect of the fine-scale structures on the coarse-scale effective permeability i.e., upscaling, is performed using a subgrid-model which includes $\delta$ as one of its parameters. A statistical inverse problem is posed to infer the weights of the Karhunen-Loève modes and $\delta$, which is then solved using an adaptive Markov Chain Monte Carlo method. The solution yields non-parametric distributions for the objects of interest, thus providing most probable estimates and uncertainty bounds on latent structures at coarse and fine scales. The technique is tested using synthetic data. The individual contributions of the static and dynamic data to the inference are also analyzed.

*Keywords:* Upscaling, Binary media, Bayesian technique, multiscale inference
*PACS:* 92.40.Kf, 05.50.Fz
*2000 MSC:* 86A32, 86A05, 76S05

*corresponding author
*Email address:* jairay@sandia.gov (J. Ray)

## 1. Introduction

Estimation of heterogeneous material properties for accurate predictions of system performance is an important problem in many fields of engineering. In particular, efficient aquifer and petroleum reservoir management require accurate knowledge of the distribution of material properties. The estimation of an unknown permeability field is arguably one of the more important challenges associated with fluid through porous media problems. This inverse form of estimation where a small number of direct measurements of the aquifer properties supplemented by measurements of the aquifer behavior under applied perturbations (e.g., injection of a tracer, transient pumping/injection, etc.) are used to estimate the aquifer properties has been an active area of research over the past 20 years [1, 2, 3, 4, 3, 5, 6, 7]. Furthermore, permeability values inherently depend on the spatial scale of the particular measurement technique. For instance, flow measurements through core plugs represent spatial scales on the order of centimeters, whereas wellbore pressure transient analyses are more on the order of hundreds of meters. This introduces a key challenge of how to accommodate measurements at different spatial scales in the inversion process. In this paper, we develop a computationally efficient stochastic inversion methodology using measurements from fine and coarse scales. The conceptual model employed here considers a binary permeability where the proportion of each phase varies in space analogous to varying proportions of sand/clay in an aquifer of fluvial origin, or varying fracture densities or levels of diagenesis in aquifers of other origin.

In this paper we present a multiscale statistical inversion technique that can be used to estimate fields (permeability/transmissivity/conductivity) from sparse observations. In particular, we show that one may be able to estimate summaries of fine-scale structures of the field, without resolving them on a mesh. While this method has been demonstrated on the estimation of 2D fields using synthetic data, the method can be extended to 3D. The 2D problem used in this paper is necessarily a compromise in the representation of the complexity of flow and transport processes (which are often strongly 3D), but it illustrates the main aspects of the inversion technique without imposing the onerous computational costs of a 3D inversion. Further, 2D inversions have a long history [1, 2] in reservoir engineering and groundwater flows, and our method adds to that literature. Practically, such 2D inversions may be applicable when one observes strong directional heterogeneity in transmissivity (horizontally) over a large (O(10 km)) domains. The method is applicable in cases where average properties can be resolved from data at one scale and discrete heterogeneities can be resolved from data collected at a finer scale.

A binary medium is one that can be adequately described in terms of inclusions of one material phase embedded in another. The two materials can have vastly different properties, and the effective behavior of the binary medium arises as a nonlinear interaction of the two constituents. Further, the proportions of the two materials need not be distributed evenly, and for situations with uneven proportions, inclusions of the less common material will exist within a continuous matrix of the other material.

Binary media exhibit complex behaviors and rich dynamics. Examples of binary media are fractured rock (with the fractures acting as high permeability inclusions), sandstone with embedded shale, and engineered composite materials. In many cases, the domain size of the binary medium (henceforth, the coarse-scale) may be a few orders of magnitude larger than the size of the inclusions and it is impractical to measure the inclusions individually. However, the length-scale contrast between the inclusion and domain size is not large enough that the inclusions can simply be homogenized i.e., a mean value for the effect of the inclusion cannot be used, but a more detailed characterization of the fine-scale is required. We call such behavior "multiscale".

This multiscale behavior raises the possibility that it may be possible to infer the characteristics of the latent fine-scale from a judicious set of measurements which inform on both the coarse and fine scales. In order to do so, a *link function* $\mathcal{L}$, that locally captures the effect of fine-scale processes and structure at the coarse-scale is required. If this function is parameterized by structural/dynamical properties of the fine-scale, it is possible to construct statistical summaries for the fine-scale. Realizations of the fine-scale that are equally consistent with observations at both scales can then be created.

We demonstrate inversion with a binary medium where the permeabilities of the two materials, $\mathcal{K}_l$ (low) and $\mathcal{K}_h$ (high), are known. The difference in permeabilities is parameterized as $\kappa = \log_{10}(\mathcal{K}_h/\mathcal{K}_l)$. We assume that we have noisy measurements of the coarse-scale effective log-permeability of the medium, $\mathbf{k}^{(obs)}$, at a few locations; they provide localized insights into the coarse-scale structure and are referred to as *static data*. We also assume that we have noisy measurements of breakthrough times, $\mathbf{t}_b^{(obs)}$, of a tracer at the same locations, from a tracer test[1]; they capture the integrated effect of fine-scale variations and are referred to as *dynamic data*. The proportion of the high permeability phase $\mathbf{F}(\mathbf{x})$ is assumed to vary in space in an unknown but smooth manner with a known covariance structure. $\mathbf{F}(\mathbf{x})$ is resolved on a relatively coarse grid and describes the spatial variation at the domain-scale. We use the grid to impose a separation of scales, and internal to a grid-box, the inclusions are modeled using a correlated Gaussian field truncated at a threshold consistent with $\mathbf{F}(\mathbf{x})$. The characteristic length of the Gaussian field, $\delta$, is defined below (and is termed a subgrid or fine-scale variable). We adopt the convention of referring to variations on the grid as being "large" or "small"; we reserve "fine" or "subgrid" for variations that are smaller than a grid-box. Together, $\mathbf{F}(\mathbf{x})$ and $\delta$ constitute a characterization of the fine-scale binary medium and their estimation from data $\mathbf{d} = \{\mathbf{k}^{(obs)}, \mathbf{t}_b^{(obs)}\}$ constitutes a statistical summary of the fine-scale. A model for generating fine scale structures

[1]We define a tracer test as follows: Water is transported through a porous medium by pumping under a steady pressure gradient. Once a velocity field has been established in the porous medium, a non-reactive tracer is injected; the advective travel time to arrive at various measurement points is called the *breakthrough* time. The exact configuration for the test is described in Sec. 4

given $\mathbf{F}(\mathbf{x})$ and $\delta$, provides realizations of the latent, unresolved fine-scale consistent with the observations.

The estimation of $\mathbf{F}(\mathbf{x})$ is posed as a Bayesian inverse problem, predicated on a forward problem $\mathcal{M}(\mathbf{K})$ that predicts the breakthrough times $\mathbf{t}_b$ at the observation locations. $\mathbf{K}_e(x)$, the effective log-permeability field, is obtained from $\mathbf{F}(\mathbf{x})$ and $\delta$ via a link function i.e. $\mathbf{K}_e(x) = \mathcal{L}(\mathbf{F}(\mathbf{x}), \delta, \kappa)$. Retention of $\delta$ in the inverse problem will allow us to evaluate the information content in the observations regarding $\delta$. To reduce the dimensionality of the inversion, we develop a reduced-order model of $\mathbf{F}(\mathbf{x})$, based on a Karhunen-Loève (KL) decomposition of a 2D field. This allows us to generate $\mathbf{F}(\mathbf{x})$, and consequently $\mathbf{K}_e(x) = \mathcal{L}(\mathbf{F}(\mathbf{x}), \delta, \kappa)$, in a parametric manner by varying $\delta$ and $\mathbf{w} = \{w_i\}, i = 1 \dots M$, where $M$ is the number of Karhunen-Loève modes retained in the reduced order model and $w_i$ are their weights. Associated predictions of $\mathbf{t}_b$ are obtained using $\mathcal{M}(\mathbf{K})$. The inverse problem is solved by sampling over the $(\mathbf{w}, \delta)$ space using an adaptive Markov Chain Monte Carlo (MCMC) technique and constructed by using a joint posterior probability density distribution $P(\mathbf{w}, \delta|\mathbf{d})$ from the samples. The use of MCMC allows us to construct posterior distributions of non-parametric shape, unlike other inversion techniques e.g., Kalman smoothers and filters, which constrain $P(\mathbf{w}, \delta|\mathbf{d})$ to be Gaussian. $P(\mathbf{w}, \delta|\mathbf{d})$ is thereafter used in posterior predictive checks, to construct fine-scale realizations of the binary medium, gather statistics on $\mathbf{K}_e(x)$ and $\mathbf{t}_b$ at the observation locations and gauge the quality of the fit of the model to data.

This paper brings two new developments to the problem of estimating an upscaled field variable e.g., permeability fields.

1. *Incorporation of the effect of unresolved scales:* Existing methods for estimating multiscale fields (e.g., zonation; see review in Sec. 2.1) involve grid-refinement under various guises – no attempt is made to incorporate structures unresolved by the grid (i.e., subgrid). In contrast, we use a statistical model to capture the effect of subgrid structures in our estimation procedure. The use of a model that has a physical, but subgrid, lengthscale as one of its parameters makes the formulation fundamentally multiscale.
2. *The use of approximate expansions to reduce dimensionality in upscaling problems:* While Gaussian process models have been used to regularize field variables (as reviewed in Sec. 2.1), few have used Karhunen-Loève expansions to reduce the dimensionality of a multiscale inverse problem. Further we use a Gaussian processes to model a *latent* variable from which the object of inference, $\mathbf{F}(\mathbf{x})$, and the observed field, $\mathbf{K}_e(x)$, are obtained via mappings. Thus, while the latent field variable is constrained to be smooth (so that it can be modeled as a Gaussian), this constraint is not necessarily extended to $\mathbf{F}(\mathbf{x})$ or $\mathbf{K}_e(x)$. In our case, $\mathbf{K}_e(x)$ contains sharp changes. This is in contrast to existing studies where the object of inference (which is also the observed field) is modeled as a Gaussian and thus required to be a smooth function.

Note that our use of a Karhunen-Loève expansion reduces the problem of estimating a field $\mathbf{F}(\mathbf{x})$ to that of inferring the values of a few parameters which are independent *a priori*. This has the convenient side-effect of allowing us to use adaptive, general-purpose (and efficient!) MCMC schemes (and software packages) in a straightforward manner. In contrast, existing MCMC-based field-estimation methods (reviewed in Sec. 2.1) use specialized blocking schemes and need to retain spatial correlations in their MCMC block proposals.

The paper is structured as follows. In Sec. 2 we review literature on the key elements of the research presented here. In Sec. 3 we describe the forward model $\mathcal{M}(\mathbf{K})$, the link function $\mathcal{L}$, and models used for reducing the dimensionality of the inverse problem. In Sec. 4, we pose the inverse problem and test the inversion technique on a problem with various types of data. In Sec. 5, we instantiate realizations of the binary fine-scale from the inferences and test their predictive skill using transport simulations i.e., breakthrough times. We draw our conclusions in Sec. 6.

## 2. Background

The estimation of field variables (permeabilities, hydraulic conductivities etc), from limited data, per se, have long been topics of active research in many science and engineering fields (see [8] and references therein); specifically for recent reviews in hydrology see [1, 2]. In this section we restrict ourselves to reviewing existing literature on the multiscale (or multilevel) inference of log-permeability modeled as random fields, methods for generating random binary fields, upscaling and models for binary media.

### *2.1. Estimation of random fields*

The use of random fields to regularize a spatial variable has been explored within the context of inferring log-permeability fields. Lee *et al.* [3] considered the estimation of spatially dependent permeability by modeling it as a random field. They estimated the permeability in each grid-block of the discretized field from dynamic data obtained from an "inverted 9 spot test". Two separate prior models were adopted for the random field to regularize the problem – a Markov random field (MRF) model with an unknown precision parameter (i.e., the precision parameter was also inferred when estimating the permeability) and a model based on Gaussian processes (GP) with a known variogram and mean permeability in the rectangular domain. Neither of the two models reduced the dimensionality of the problem i.e., the number of parameters being estimated was equal to the size of the Cartesian mesh, which ranged between $32^2$ and $64^2$. This work required specialized updating schemes to improve mixing in the Metropolis-Hastings sampler used to construct the posterior distribution of the permeability field. MRF priors were also used by Wang *et al.* [4] when estimating the initial (spatial) distribution of a contaminant within a porous medium. The contaminant was transported by groundwater flows and time-variant

concentration measurements were available at a few locations. They employed a hierarchical Bayesian formulation to estimate the concentration distribution as well as the precision of the MRF model and the variance of the measurement error. As in [3], no attempt was made to reduce the dimensionality of the inference problem. Fu and Gómez-Hernández [5, 6] present a more recent example of the use of MCMC with blocked-updating when inferring log-permeability fields. Unlike Lee *et al.* [3] where a red-black decomposition of grid-blocks was used to update the log-permeability field (modeled as a MRF) in the MCMC, they used a multiGaussian representation for the object of inference and devised a specialized technique for constructing the proposal within the MCMC. In particular, they divided the grid-blocks in the Cartesian mesh into concentric "strips", which were updated together as a block; the proposals for the blocks were obtained by kriging.

The need for explicit regularization can be eliminated if one can represent the field to be estimated using a low-dimensional model. If the object of inference can be modeled as a multivariate Gaussian field, a truncated Karhunen-Loève expansion can be used. In [7], Li *et al.* consider estimation of the log-conductivity distribution of a reservoir from measurements of the steady-state hydraulic heads by preserving 400 terms in the Karhunen-Loève expansion. Application of Karhunen-Loève expansion to provide a reduced-order model for a random field was also used by Marzouk *et al.* in [9] to estimate a log-diffusivity field within the context of a 1D thermal transport problem, with time-dependent temperature measurements at a few sensor points. They found that the Karhunen-Loève expansion based on the *prior* covariance of the log-diffusivity field was remarkably accurate for representing its *posterior* distribution, conditioned on the observations. In [10], Jafarpur and Mclaughlin compare the use of a Karhunen-Loève transform versus the discrete cosine transform (DCT) and find the latter to be more computationally efficient, if slightly less accurate. In [11] they couple the reduced order DCT model to an ensemble Kalman filter to infer permeability fields as well as reservoir states via history matching. In [12], they use the discrete cosine bases as a *sparse* representation for the log-permeability field and infer their value *as well as the sparsity pattern* via history matching.

Multiscale/multilevel inversion techniques explicitly recognize the existence of more than one scale and employ different types of data across scales. These techniques generally involve solving the inverse problem at different levels of discretizations , (i.e., on a multilevel mesh), with conditioning relations (i.e., upscaling and downscaling functions) to link scales together [13, 14]. Multiscale solutions primarily differ in the complexity of the conditioning relations and whether the multiscale inference requires iteration between scales. Other techniques run separate MCMC chains using coarse and fine-scale models, with periodic swaps of parameters between them [15, 5], or use a fast coarse-scale (or approximate model) as a preconditioner/filter for proposals (inside an MCMC chain), prior to computing the posterior with a finely-resolved forward model [16, 17, 5]. These approaches exploit Christen and Fox's [18] approach of using a computationally inexpensive approximation of a model (in this

case, a low-resolution forward model) to efficiently explore a parameter space (alternatively, MCMC proposals). Note that these methods require explicit definition of coarse, fine and if necessary, intermediate scales. On the other hand, "zonation" methods [19, 20, 21, 22] adopt a continuous-level-of-detail approach to inference and in the process combine elements of dimensionality reduction and multiscale inference.

We borrow the approach adopted in [9, 16, 17] and use Karhunen-Loève expansions to reduce the dimensionality of the inverse problem. We apply them here to the spatially varying $\mathbf{F}(\mathbf{x})$ which is then input to the link function providing an effective permeability informed from both scales. Instead of using a multilevel inversion technique, we assume that a sufficient contrast exists between the resolution at which we perform the inference and the size of individual fine-scale/subgrid structures that a complete description of the fine-scale is not very useful. However, we adopt the practice, common in multiscale inversion, of enforcing scale separation using a grid.

### *2.2. Topological and upscaling models for random binary media*

A key component of our inversion scheme is a link function that upscales subgrid structures. Upscaling models can be categorized approximately into (a) models that seek to estimate an effective permeability/conductivity of the media and (b) models that seek to generate geometries/realizations of such media. We will not address models for fractured media, since the fractures may sometimes be as long as the domain.

#### *2.2.1. Models for estimating permeability*

There has been considerable work in estimating the effective permeability of a random, porous binary medium. Effective medium theories (EMT) for binary assemblages [23, 24, 25, 26, 27, 28, 29, 30, 31, 32], seek to calculate a representative permeability as a function of the permeabilities of the two components and their relative abundances. Reviews and comparisons to other methods can be found in [33, 34]. EMT-like approaches assume non-interaction between inclusions and work best when the inclusion proportion is small [35, 33]. In contrast, Knudby *et al.* [34] have developed a model for estimating the effective permeability of a binary medium which *does* consider the interaction of inclusions. It does so by using an average inter-inclusion distance as a proxy for the average length of a flowpath through the low conductivity component. However, Knudby et al.'s model, taken as-is, requires creation of a realization of the binary medium so that the geometrical parameters (viz., the inclusion size and the inter-inclusion distance) may be calculated.

#### *2.2.2. Models for the geometry of random binary media*

A very common means of generating representations of random media with multiple components is via indicator variables which choose between the components. Indicator geostatistical techniques [36] do so via a variogram to define spatial variations [37, 38, 39] or via transition probabilities between indicator classes [40, 41]. Less common means of generating spatial binary media are object-based and Boolean

models [42] and random media models based on pluriGaussian and truncated multiGaussian fields [42, 43].

The development of excursion set theory, as applied to multiGaussian fields, has mostly occurred in medical imaging and astrophysics [44, 45, 46]. In particular, given a *definition* of a multiGaussian field (note, *not* a realization), it is possible to analytically calculate expected values of the total area, the number of distinct excursions and the average excursion size above a given threshold [47, 48, 49]. These ideas have also been employed in porous media flows - Phillips and Wilson [50] proposed mean threshold crossing distances to estimate correlation lengths of permeability. In [51], the authors of the current paper modeled a random binary medium as a truncated multiGaussian field and used excursion set theory to estimate expected values for inclusion size and number. These were the incorporated into an upscaling model derived from Knudby *et al.* [34] (see Sec. 3.3). The model is analytical and sufficiently efficient for use in an inference scheme based on MCMC sampling.

### *2.3. Adaptive Markov chain Monte Carlo techniques*

Our inversion process is based on an adaptive MCMC techniques and although we do not offer any algorithmic advancements, a brief background of MCMC techniques is presented for completeness. In recent years, MCMC techniques have been increasingly used to fit models to observations [52], since they allow estimation of parameters while simultaneously quantifying the uncertainty in the estimate. Further, they place no restrictions on the probability distributions of the estimated parameters. Metropolis-Hastings (MH) samplers [52] are commonly used since they place no restrictions on the kind of models, the type of likelihood expressions or the priors used in posing the inverse problem. Blockwise updates, when a number of (or all) parameters are updated at once are typically used when estimating field quantities [53, 54, 3, 52, 55, 5].

Adaptive Metropolis [56, 53] (AM) is a variation of the MH sampler which uses a *global* adaptive strategy to perform online tuning of the current proposal to increase mixing and acceptance rates. AM starts with a pre-specified proposal density but periodically recalculates an empirical posterior covariance based on the samples collected up to that point. The covariance asymptotically resembles that of the posterior. The technique is neither Markovian nor reversible and in [53] the authors identify the conditions under which AM will recover the desired stationary distribution. Delayed rejection [57, 58, 59] is a *local* MH variation that combines different proposals. An MH sampler is started with a rather large proposal covariance. When a proposal is rejected, the initial covariance is scaled down by a uniform factor, and tried again rather than simply advancing in the sample path (hence delayed rejection, DR). DR has been shown to outperform MH [56]. Delayed Rejection Adaptive Metropolis (DRAM), the MCMC technique used here, is an amalgamation of the AM and DR [54]. DRAM is non-Markovian and provably ergodic, i.e., it yields asymptotically unbiased estimators [54].

## 3. Models used in the inverse problem

In this section we describe the models used in our inverse problem. We first describe $\mathcal{M}(\mathbf{K})$, a porous media transport model which serves as the forward problem in the inversion. Subsequently, we discuss the Karhunen-Loève expansions of random fields which are used to reduce the dimensionality of the inverse problem. Finally, we review the link function $\mathcal{L}$ that summarizes the impact of subgrid structures.

### *3.1. The transport model $\mathcal{M}(\mathbf{K})$*

$\mathcal{M}(\mathbf{K})$ is a 2D Darcy-flow model for the transport of an inert tracer through a saturated porous medium by an incompressible, single-phase fluid. Given a coarse-scale log-permeability field $\mathbf{K}$, appropriate initial and boundary conditions (including a steady-state pressure gradient and a fluid source and sink inside $\mathcal{D}$), the model calculates a steady state velocity field and advects a tracer (treated as a passive scalar) through it to obtain breakthrough times $\mathbf{t}_b$ at a set of $N_s$ "sensor" locations inside $\mathcal{D}$.

As shown in Fig. 1(a), we consider a 2D domain $\mathcal{D}$ with no-flow boundary conditions imposed on $\partial\mathcal{D}$. We consider a log-permeability field $\mathbf{K}$ defined on $\mathcal{D}$. An incompressible fluid, with viscosity $\mu$ is pumped in at the lower left corner and pumped out at an equal rate at the upper right. In this problem, we will ignore the effect of gravity. Therefore, via Darcy's model for porous media flows, the velocity $\mathbf{v}$ is given by

$$\mathbf{v} = \frac{\mathcal{K}}{\mu}\nabla p, \qquad \nabla \cdot \mathbf{v} = \nabla \cdot \frac{\mathcal{K}}{\mu}\nabla p = \frac{q}{\rho} \tag{1}$$

where $p$ is the pressure field defined on $\mathcal{D}$, $q$ is the strength of the source/sink and $\rho$ is the density of the fluid. The equation is solved using the second-order finite-volume scheme described in [60], on a uniform mesh. Two-point flux approximations are used, and the permeability at the interface of adjacent grid-blocks are estimated by a harmonic average. A solution of these equations, for an injection-production well pair in a binary medium, is shown in Fig. 1(b). The light areas denote high-permeability material and the dark regions are low-permeability. A few streamlines, flowing from bottom left to top right, are plotted in Fig. 1(b). The local permeability is considered isotropic, and the permeability $\mathcal{K}$ is modeled as a 2D field rather than a full tensor. The proportion of high-permeability material $\mathbf{F}(\mathbf{x})$ and the true effective (upscaled) log-permeability are shown in Fig. 1 (c) and (d). Note that the $\mathbf{K}_e(x)$ field shows a rougher distribution and significantly more structure than $\mathbf{F}(\mathbf{x})$.

Solving (1) for $p$ yields the velocity $\mathbf{v}$ at the centers of the grid-block edges i.e., the velocities are obtained on a staggered mesh. This is used to advect the passive scalar, using the model in (2),

$$\frac{\partial c}{\partial t} + \mathbf{v} \cdot \nabla c = q_c \tag{2}$$

where $c(\mathbf{x})$ is the concentration field of a tracer and $q_c$, non-zero only at the lower left and upper right corners of $\mathcal{D}$, is the source and sink for the tracer. The concentration of the tracer at the source, $c_{source}$, is set to 1 and $q_{c,source}$ is set equal to the flux of the fluid. The tracer flux at the sink, $q_{c,sink}$, is obtained by multiplying the fluid outflow with the local tracer concentration, $c_{sink}(t)$, which increases in time until it reaches the source value of 1.0. (2) was solved on the same Cartesian mesh as (1), using an upwind second-order, finite-volume scheme [61]. Tracer concentrations were monitored at two sets of sensor locations (set A with 20 sensors and B with 34) as shown in Fig. 1(e) and (f); the time $t_b$ at which $c = 0.5$ was achieved at any given sensor was denoted as its breakthrough time. Note that (2) does not model pore-scale dispersion or molecular diffusion of the tracer.

### *3.2. Karhunen-Loève expansions of random fields*

The inversion process targets permeability which lives in the space of the entire computational domain. For production quality reservoir or groundwater studies this introduces very high dimensional spaces which are computationally intractable to solve with MCMC methods. An appropriate parameterization is therefore necessary and although there are many to choose from, the KL expansion is the optimal since it minimizes the mean squared error when used to represent a stochastic process.

Let $R(\mathbf{x}, \omega)$ be a real-valued random field with zero mean, finite second moments and covariance function that is continuous in $\mathcal{D} \times \mathcal{D}$. $\omega \in \Omega$, where $\Omega$ is a sample space and $R(\mathbf{x}, \omega)$ can be considered to be a collection of real-valued random variables, indexed by $\mathbf{x} \in \mathcal{D}$, $\mathcal{D}$ being a bounded spatial domain. Then, the Karhunen-Loève expansion of $R(\mathbf{x}, \omega)$ can be written as $R(\mathbf{x}, \omega) = \sum_{i=1}^{\infty} w_i(\omega)\sqrt{\lambda_i}\phi_i(\mathbf{x})$. This equality holds in the pointwise and mean-square sense; convergence is in $L^2(\Omega)$ for all $\mathbf{x} \in \mathcal{D}$. Further, if $R(\cdot)$ is Gaussian and almost surely continuous, then the convergence is uniform in $\mathcal{D}$ with probability 1 [62]. $\lambda_i$ and $\phi_i(\mathbf{x})$ are the eigenvalues and eigenfunctions of the covariance kernel $C(\mathbf{x}, \mathbf{y})$

$$\int_{\mathcal{D}} C(\mathbf{x}_1, \mathbf{x}_2)\phi_i(\mathbf{x}_2)d\mathbf{x}_2 = \lambda_i\phi_i(\mathbf{x}_1). \tag{3}$$

Since $R(\cdot)$ is assumed Gaussian, the covariance kernel $C(\mathbf{x}, \mathbf{y})$ is symmetric and positive semi-definite and so, by [63], $C(\mathbf{x}_1, \mathbf{x}_2) = \sum_{i=1}^{\infty} \lambda_i\phi_i(\mathbf{x}_1)\phi_i(\mathbf{x}_2)$ where $\phi_i(\mathbf{x})$ are continuous functions and form an orthonormal system in $L^2(\mathcal{D})$. Also, $w_i \sim \mathsf{N}(0, 1)$ and independent of each other.

In order to reduce the dimensionality of our inverse problem, we will model fields with a truncated Karhunen-Loève series. In such a case, the approximate field $R_M(\cdot)$ and its covariance function can be represented as

$$R_M(\mathbf{x}, \omega) = \sum_{i=1}^{M} w_i(\omega)\sqrt{\lambda_i}\phi_i(\mathbf{x}), \qquad C_M(\mathbf{x}_1, \mathbf{x}_2) = \sum_{i=1}^{M} \lambda_i\phi_i(\mathbf{x}_1)\phi_i(\mathbf{x}_2)$$

The total variance or "energy" of $R_M(\cdot)$ is given by

$$\int_{\mathcal{D}} E(R_M(\mathbf{x},\omega)^2)d\mathbf{x} = \int_{\mathcal{D}} C_M(\mathbf{x},\mathbf{x})d\mathbf{x} = \sum_{i=1}^{M} \lambda_i^2 \tag{4}$$

*3.3. The link function $\mathcal{L}$*

Analogous to the motivation for a KL parameterization of permeability, the MCMC based inversion process cannot afford to process any dynamics at the fine scale. To this end, our coarse scale inversion is endowed with a *link function* ($\mathcal{L}(\mathbf{F}(\mathbf{x}),\delta,\kappa)$) that estimates the effect of unresolved inclusions on the log-permeability of a grid-block. Note that $(\mathbf{F}(\mathbf{x}),\delta)$ is an incomplete specification of the fine-scale structures that may reside within a grid-block and consequently an infinite number of realizations (i.e., an ensemble) of the fine-scale may be conditioned to it. The link function $\mathcal{L}$, being deterministic, maps the entire ensemble of binary field realizations to the same effective permeability $\mathbf{K}_e$, and in doing so incurs an upscaling error. The precise upscaling procedure, called truncated Gaussian–distance based upscaling (TG–DBU) is described in detail in [51].

TG–DBU starts with a model of the binary medium inside a grid-block. The medium is modeled as a standard-normal, multiGaussian random field. The multi-Gaussian field, in turn, is created by convolution of an uncorrelated white-noise field with a Gaussian kernel. The size of the kernel is defined by its full-width at half maximum (FWHM) value, which also defines the correlation length of the resulting random field: $\delta = \sigma\sqrt{8\ln 2}$. We truncate the correlated multiGaussian field at a threshold $w$, to create a set of discrete, irregularly-shaped plateaus. We use the convention that values lesser than (or equal to) $w$ define the high permeability regions and values greater than $w$ are the low permeability regions. Knudby *et al.* [34] provide a model for the effective permeability of the binary field as a function of (1) the fraction of high-permeability material $\mathbf{F}$, (2) an area weighted average distance between high permeability regions along the direction of flow (called $\overline{D_{norm}}$), and (3), the log-permeabilities of the two components of the binary medium, $\mathcal{K}_l$ and $\mathcal{K}_h$. $\overline{D_{norm}}$ can be calculated from a fully-resolved realization of the binary medium; however, this can become expensive if the binary medium, and operations on it, are to be performed on a fine mesh. Instead, we use the model developed by McKenna *et al.* [51] that combines point process theory, the Euler characteristic and expectation properties of excursion sets of truncated Gaussian fields to estimate $\overline{D_{norm}}$. The complete random binary field is never instantiated. The estimates of $\overline{D_{norm}}$ so developed are used in the upscaling expressions in [34] to calculate effective log-permeability at the coarse scale, $\mathbf{K}_e$. The upscaling expressions are functions of $\mathbf{F}(\mathbf{x}),\delta$ and $\kappa$ in a grid-block. Additional details on this link function can be found in [51].

Note that the log-permeability $\mathbf{K}_e = \mathcal{L}(\mathbf{F},\delta,\kappa)$ provided by TG–DBU is a point approximation of the distribution of log-permeabilities consistent with $\mathbf{F}$, $\delta$ and $\kappa$. In Fig. 2 (left), we plot the effective log-permeabilities for $\mathcal{K}_l = 1, \mathcal{K}_h = 100$ and $\delta$

of 37.7 grid-cells (in a domain of $500 \times 500$ grid-cells) as predicted by our model, $\mathcal{L}$. We also plot the numerically evaluated log-permeabilities corresponding to 30 binary field realizations having the same $\{\mathbf{F}, \delta\}$ with points, forming a cloud around $\mathbf{K}_e(x) = \mathcal{L}(\mathbf{F}, \delta, \kappa)$. Note that the model predicts $\mathbf{K}_e(x)$ for all $\mathbf{F}$, but slightly underestimates it. In Fig. 2 (right) we show the variation of $\mathbf{K}_e$ as a function of $\delta/\Delta$, where $\Delta$ is the grid-block size. The assumptions underlying $\mathcal{L}$ dictate that $\delta/\Delta \ll 1$. The break in the log-permeability predictions $\mathcal{L}(\mathbf{F}, \delta, \kappa)$ at $\mathbf{F} \approx 0.5$ is due to application of the phase interchange theorem [64] as part of $\mathcal{L}$ that provides consistent upscaling of inclusions of either material within the other. Additionally, this break also accounts for non-linear percolation effects i.e., the high permeability phase exists in a connected region large enough to span the domain, see [51]. Further, the high-permeability inclusions increase the effective permeability far more (when $\mathbf{F} < 0.5$) when they are finely dispersed (smaller $\delta$ and consequently $\overline{D_{norm}}$), compared to their effect when they exist as large, but isolated, entities.

The scaling function, $\mathcal{L}$, used here is unique among binary media scaling functions in that it incorporates $\mathbf{F}$, $\delta$ and $\kappa$ into estimates $\mathbf{K}_e$. However, the impact of $\delta$ on the resulting $\mathbf{K}_e$ values is enhanced in the areas with $\mathbf{F}$ near 0.50, where the effective permeability can display a discontinuous change. This is because when the high- and low-permeability phases are in approximately equal proportions, a slight change in $\delta$ can establish long, high-permeability channels inside a grid-block, drastically changing its effective permeability (i.e., the high permeability phase reaches the percolation threshold). This change can be very significant if the inclusions exist as large, but barely disconnected, entities. This sensitivity quickly degrades as $\mathbf{F}$ moves away from 0.5. Practically, $\Delta$ denotes the grid-box size of the mesh that we will use in this work to discretize a domain, and thus $\mathcal{L}$ acts as a subgrid model for the structures that the grid will not resolve.

In the rest of the paper, we will use $\mathbf{K}_e(x)$ as a deterministic approximation for the log-permeabilities and model the discrepancy between observations of log-permeability and model predictions as simple i.i.d. Gaussians (homoscedastic errors). While the choice of the error model (Gaussian versus a more involved one) does not detract from the general characteristics of an inference procedure, it does impact the accuracy of the estimates/inferences.

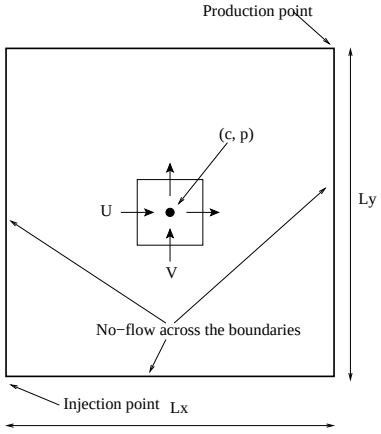


(a) Domain

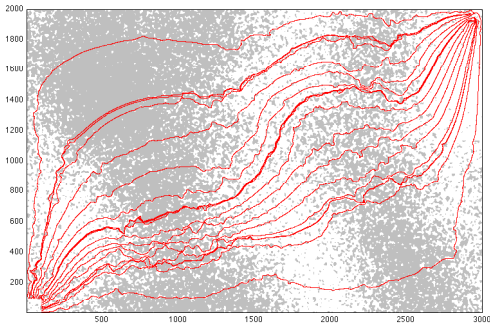

(b) Fine-scale

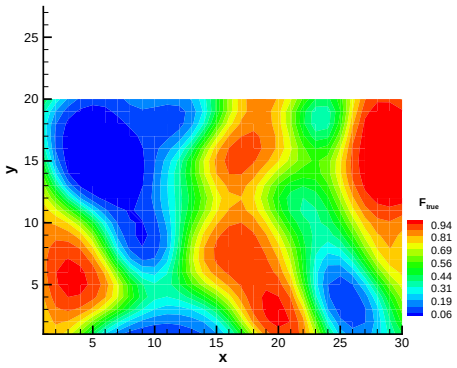


(c) Proportionality field $\mathbf{F}(\mathbf{x})$

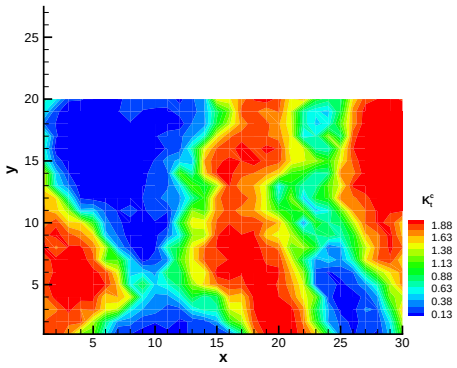


(d) The true $\log_{10}(\mathbf{K}_e(x))$ field

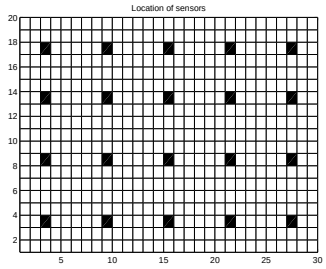


(e) SSA

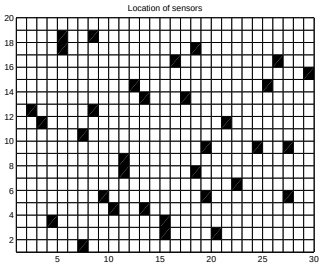


(f) SSB

Figure 1: (a) The 2D rectangular domain $\mathcal{D}$ with associated dimensions. No-flow boundary conditions are defined on $\partial\mathcal{D}$. A grid-block showing the collocation for pressure $p$ and the velocities $(u, v)$ in the x- and y-directions is shown. (b) We show a schematic of a binary medium higher permeability (white) and lower permeability (gray). Individual inclusions of either material in the other are visible. (c) The true $\mathbf{F}_c^t(\mathbf{x})$ field for the proportion of inclusions. (d) The true upscaled log-permeability field $\mathbf{K}_c^t$. (e) The $30 \times 20$ coarse-scale computational mesh with the locations of 20 sensors (sensor-set A, SSA). (f) We show the locations of the 34 sensors in sensor-set B (SSB).

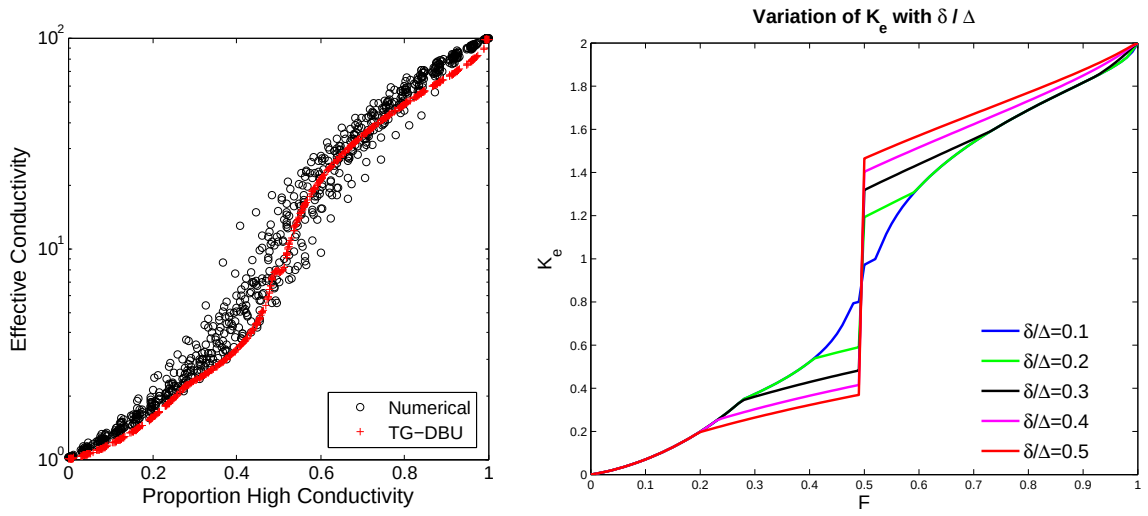


Figure 2: Left: Plot of $\mathbf{K}_e$ calculated using the link function $\mathcal{L}$, (labeled: TG-DBU) compared to $\mathbf{K}_e$ calculated numerically from 30 random binary fields as a function of $\mathbf{F}$. These results were calculated for a square domain with length, $\Delta = 500$ units and $\delta$ is 37.7 ($\delta/\Delta = 0.075$). Right: Variation of $\mathbf{K}_e$ as a function of $\delta/\Delta$.

## 4. Multiscale inference

In this section, we pose and solve an inverse problem using the models described in Sec. 3. Specifically, we explore the ability of the observations to constrain the inference of structures at two spatial scales, the relative contributions of the static and dynamic data and the effect of increasing the number of observations. We also demonstrate sampling of the posterior distribution to generate fine-scale realizations which are consistent with the observations.

### *4.1. Posing the inverse problem*

Consider that the domain $\mathcal{D}$ is 2D, rectangular, of size $L_x \times L_y$, and discretized by a Cartesian mesh of resolution $N_x \times N_y$. Consider a spatially variable field $\boldsymbol{\zeta}(\mathbf{x})$, $-\infty < \boldsymbol{\zeta}(\mathbf{x}) < \infty$ defined on $\mathcal{D}$. We model $\boldsymbol{\zeta}(\mathbf{x})$ as a random field using a Gaussian Process, i.e., the discrete form of $\boldsymbol{\zeta}(\mathbf{x})$, the vector $\boldsymbol{\zeta}$, is a random variable with multivariate Gaussian distribution and a known covariance matrix $\boldsymbol{\Gamma}$. We further specify that the inclusion proportion $\mathbf{F}(\mathbf{x})$ is an analytical function of $\boldsymbol{\zeta}(\mathbf{x})$. $\mathbf{F}(\mathbf{x})$ governs the predicted effective log-permeability $\mathbf{K}_e(x)$ and breakthrough time $\mathbf{t}_b$ via models $\mathcal{L}(\mathbf{F}(\mathbf{x}), \delta)$ and $\mathcal{M}(\mathbf{K})$. These relationships are summarized in (5)

$$\begin{aligned}
\boldsymbol{\zeta} &\sim \mathsf{N}(0, \boldsymbol{\Gamma}), \\
\boldsymbol{\Gamma}_{ij} &= C(\mathbf{x}_i, \mathbf{x}_j) = a \exp(-|\mathbf{x}_i - \mathbf{x}_j|^2 / b^2), \\
\mathbf{F}(\mathbf{x}) &= \frac{1}{2}\left(1 + \operatorname{erf}\left(\frac{\boldsymbol{\zeta}(\mathbf{x})}{\sqrt{2}}\right)\right), \\
\mathbf{K}_e(x) &= \mathcal{L}(\mathbf{F}(\mathbf{x}), \delta, \kappa), \\
\mathbf{t}_b &= \mathcal{M}(\mathbf{K}_e(x))
\end{aligned} \tag{5}$$

where $\boldsymbol{\Gamma}_{ij}$, an element of the covariance matrix $\boldsymbol{\Gamma}$, denotes the correlation between grid-blocks $i$ and $j$ in the mesh. The scale $a$ and range $b$ of the covariance kernel are assumed known. Note that the analytical transformation $\boldsymbol{\zeta} \mapsto \mathbf{F}(\mathbf{x})$ is required to map $\mathbf{F} \in [0, 1]$ to $\boldsymbol{\zeta} \in [-\infty, \infty]$, so that a Gaussian model may be used. The inference does not depend on the particular transformation in (5); any transformation that allows the use of Gaussian fields (and consequently, a Karhunen-Loève decomposition) may be used.

Given a set of noisy data $\mathbf{d} = \{\mathbf{k}^{(obs)}, \mathbf{t}_b^{(obs)}\}$ at a set of $N_s$ "sensor" points, we wish to infer the posterior distribution $P(\mathbf{F}(\mathbf{x}), \delta|\mathbf{d})$. Using Bayes' formula, this can be written as

$$\underbrace{P(\mathbf{F}(\mathbf{x}), \delta|\mathbf{d})}_{Posterior} \propto \underbrace{P(\mathbf{d}|\mathbf{F}(\mathbf{x}), \delta)}_{Likelihood} \underbrace{\pi(\mathbf{F}(\mathbf{x}), \delta)}_{Prior} \tag{6}$$

where $\pi(\cdot)$ denotes our prior belief regarding the distribution of a variable. We model the discrepancy between the data $\mathbf{d}$ and model predictions as Gaussian residuals, i.e.,

$$\mathbf{k}^{(obs)} - \mathbf{K}_e(x) = \mathbf{k}^{(obs)} - \mathcal{L}(\mathbf{F}(\mathbf{x}), \delta, \kappa) = \mathbf{e}_k \sim \mathsf{N}(\boldsymbol{\mu}_k, \boldsymbol{\Gamma}_k),$$

$$\mathbf{t}_b^{(obs)} - \mathbf{t}_b \;=\; \mathbf{t}_b^{(obs)} - \mathcal{M}(\mathbf{K}_e(x)) = \mathbf{e}_t \sim \mathsf{N}(\boldsymbol{\mu}_t, \boldsymbol{\Gamma}_t), \tag{7}$$

where $\boldsymbol{\mu}_k, \boldsymbol{\mu}_t$ are the means of the discrepancy between observed and model (i.e., predicted) log-permeabilities and breakthrough times and $\boldsymbol{\Gamma}_k, \boldsymbol{\Gamma}_t$ the corresponding error covariances respectively. Under these error-modeling assumptions, (6) reduces to

$$\begin{aligned} P(\mathbf{F}(\mathbf{x}), \delta|\mathbf{d}) &\propto P(\mathbf{d}|\mathbf{F}(\mathbf{x}), \delta)\pi(\mathbf{F}(\mathbf{x}), \delta) \\ &\propto \exp\left(-[\mathbf{e}_k - \boldsymbol{\mu}_k]^T \boldsymbol{\Gamma}_k^{-1} [\mathbf{e}_k - \boldsymbol{\mu}_k]\right) \exp\left(-[\mathbf{e}_t - \boldsymbol{\mu}_t]^T \boldsymbol{\Gamma}_t^{-1} [\mathbf{e}_t - \boldsymbol{\mu}_t]\right) \\ &\quad \pi(\mathbf{F}(\mathbf{x}), \delta), \end{aligned} \tag{8}$$

We assume that the discrepancies $\mathbf{e}_k$ and $\mathbf{e}_t$ are independent and model them as i.i.d. Gaussians with constant standard deviations i.e.,

$$\boldsymbol{\Gamma}_k = \sigma_k^2 \mathbf{I}; \qquad \boldsymbol{\Gamma}_t = \sigma_t^2 \mathbf{I}.$$

where $\mathbf{I}$ is the identity matrix. This is equivalent to stating that there are no systematic discrepancies between observations and model predictions as a function of $\mathbf{F}(\mathbf{x}), \delta$ and $\kappa$. Given the relationship between $\mathbf{K}_e(x), \mathbf{F}(\mathbf{x})$ and $\boldsymbol{\zeta}$ (5), and the modeling assumptions regarding errors, (8) can be compactly written in terms of $\boldsymbol{\zeta}$ as

$$\begin{aligned} P(\boldsymbol{\zeta}, \delta|\mathbf{d}) &\propto P(\mathbf{d}|\boldsymbol{\zeta}, \delta)\pi(\boldsymbol{\zeta})\pi(\delta) \\ &\propto \exp\left(-\frac{[\mathbf{e}_k(\boldsymbol{\zeta}, \delta) - \boldsymbol{\mu}_k]^T [\mathbf{e}_k(\boldsymbol{\zeta}, \delta) - \boldsymbol{\mu}_k]}{\sigma_k^2}\right) \\ &\quad \exp\left(-\frac{[\mathbf{e}_t(\boldsymbol{\zeta}, \delta) - \boldsymbol{\mu}_t]^T [\mathbf{e}_t(\boldsymbol{\zeta}, \delta) - \boldsymbol{\mu}_t]}{\sigma_t^2}\right) \\ &\quad \pi(\boldsymbol{\zeta})\pi(\delta). \end{aligned} \tag{9}$$

Here, we have also assumed that the prior distributions of $\delta$ and $\boldsymbol{\zeta}$ are independent.

Solving the inverse problem in (9) would require us to infer each of the elements of $\boldsymbol{\zeta}$ (though constrained by $\boldsymbol{\Gamma}$); the dimensionality of the inverse problem is $N_x \times N_y$, which can be extremely large depending on the mesh. In order to reduce the dimensionality of the inverse problem, we appeal to the discussion in Sec. 3.2 and construct a low-dimensional model of $\boldsymbol{\zeta}(\mathbf{x})$ using a Karhunen-Loève expansion.

$$\boldsymbol{\zeta}_M = \sum_i^M w_i \sqrt{\lambda_i} \phi_i, \quad \text{with} \quad w_i \sim \mathsf{N}(0, 1), \tag{10}$$

where $\lambda_i$ are the eigenvalues of the covariance matrix $\boldsymbol{\Gamma}$, $\phi_i$ the corresponding eigenvectors, and $w_i$ the weights which are modeled as i.i.d standard normals due to the Gaussian Process model for $\boldsymbol{\zeta}$. In this expansion, we retain the $M$-largest eigenmodes. Note that by (4), the variance of the approximate field is less than the original one,

and inferences will tend to be smoother than the true field. The link between the Karhunen-Loève weights $\mathbf{w}$ and $\mathbf{t}_b$ can be succinctly written as

$$\mathbf{w} \xrightarrow{\text{KL modes}} \boldsymbol{\zeta} \xrightarrow{(5)} \mathbf{F}(\mathbf{x}) \xrightarrow{\mathcal{L},\delta,\kappa} \mathbf{K}_e(x) \xrightarrow{\mathcal{M}(\mathbf{K})} \mathbf{t}_b \tag{11}$$

Replacing $\boldsymbol{\zeta}$ in (9) with its Karhunen-Loève expansion (10), we get

$$\begin{aligned} P(\mathbf{w},\delta|\mathbf{d}) \quad \propto \quad & \exp\left(-\frac{[\mathbf{e}_k(\mathbf{w},\delta)-\boldsymbol{\mu}_k]^T[\mathbf{e}_k(\mathbf{w},\delta)-\boldsymbol{\mu}_k]}{\sigma_k^2} - \frac{[\mathbf{e}_t(\mathbf{w},\delta)-\boldsymbol{\mu}_t]^T[\mathbf{e}_t(\mathbf{w},\delta)-\boldsymbol{\mu}_t]}{\sigma_t^2}\right) \\ & \pi(\delta)\prod_{l=1}^{M}\exp(-w_l^2). \end{aligned} \tag{12}$$

Here, the prior on $\mathbf{w}$, $\pi(\mathbf{w})$, has been expressed in terms of its independent elements, $w_i$, whose priors are standard normals. The objects of inference are the $M$ elements of $\mathbf{w}$ and $\delta$. Note that the dimensionality of the inverse problem is no longer directly dependent on the mesh used for the inversion.

We will assume that the porosity of the binary medium is a constant in space and time, and is known. The basis for this assumption is the observation that variations in $\mathbf{K}$ for most porous media are much larger than variations in porosity.

### *4.2. Solving the inverse problem*

In this section, we solve (12) to develop a multi-dimensional posterior distribution from which we develop realizations of both the fine- and coarse-scale fields that are consistent with the data. We first describe how we develop the "ground-truth" binary field (fine-scale), followed by the generation of the synthetic data that serve as observations, the development of the posterior distribution $P(\mathbf{w},\delta|\mathbf{d})$ and finally, by an analysis of the inversion methodology.

#### *4.2.1. Development of the "ground-truth" fine-scale binary field*

The domain $\mathcal{D}$ is dimensioned as $L_x = 1.5, L_y = 1.0$. The covariance of the $\boldsymbol{\zeta}$ field is initialized with $a = 1.0, b = 0.1(L_x^2 + L_y^2)^{1/2}$ (see (5)). $\boldsymbol{\zeta}$ is modeled as a multiGaussian field and a realization is obtained on a coarse $30 \times 20$ mesh of grid-blocks on $\mathcal{D}$. The "true" high-permeability proportions on the coarse mesh, $\mathbf{F}_c^t(\mathbf{x})$, are calculated using the transformation in (5). Each grid-block is thereafter further refined into $100 \times 100$ *grid-cells*, leading to a $3000 \times 2000$ grid-cell discretization of $\mathcal{D}$. The domain has a unit height. While there is a two-order-of-magnitude change between the fine and coarse scales, we keep the multiscale approach here completely general by purposefully omitting any assignment of an absolute scale to the description of the ground truth.

We generate a random binary field on the $3000 \times 2000$ mesh per the procedure in Sec. 3.3 and [51]. We initialize the mesh with white noise and convolve it with a

Gaussian kernel with $\sigma = 5.0$ ($\delta = 11.774$) grid-cells. $\mathbf{F}(\mathbf{x})$, the proportion of high-permeability material in each grid-block is used to calculate the threshold $w$. The $w-level$ excursion set creates the random inclusions in each grid-block. Repeated over all coarse-scale grid-blocks, we obtain the fine-scale binary medium on a $3000 \times 2000$ grid. The high and low permeability materials are assigned permeabilities of $\mathcal{K}_h = 100$ and $\mathcal{K}_l = 1$ ($\kappa = 2$).

*4.2.2. Generation of synthetic data*

The synthetic data consist of measurements $\mathbf{k}^{(obs)}$ of effective log-permeability of the coarse grid-blocks containing the sensors. Data for two sets of sensors, SSA and SSB (see sensor locations in Figure. 1, e and f), are available. The permeabilities are calculated by solving a permeameter boundary condition problem using the true fine-scale permeabilities for each of the coarse grid-blocks. For each grid-block, a time-independent pressure difference is imposed in one direction, and zero-outflow in the perpendicular one to calculate a flow-rate. The resulting flux is used to calculate the effective grid-block permeability in that direction. The directions of pressure difference and zero-outflow are then exchanged to obtain the permeability in the perpendicular direction. The two permeabilities so calculated are similar and the geometric mean of the permeabilities is taken as the "upscaled" permeability of the binary medium in that grid-block. Flow simulations for each of the grid-blocks in the $30 \times 20$ mesh are performed with MODFLOW-2005 [65]. We refer to the resulting log-permeability field as the true, upscaled log-permeability field, $\mathbf{K}_c^t$. Those values that correspond to the sensor grid-blocks in the SSA and SSB sets form the static data, $\mathbf{k}^{(obs)}$. Gaussian observation errors ($\sim \mathsf{N}(0, \{0.1\}^2)$, i.i.d.) are added to them. Note that while we have used permeameter boundary conditions to calculate synthetic observations of effective permeability at sensor grid-blocks, there are other ways of estimating effective permeability around a well (e.g., various well testing and interpretation methods). Further, each of these methods of estimating a "point-wise" permeability has its own associated measurement error. This is an involved topic and beyond the scope of this paper.

The original random binary field, on the $3000 \times 2000$ mesh, is then subjected to a tracer transport simulation, as described in Sec. 3.1. MODPATH [66] is a Lagrangian particle tracking method operating on flux fields calculated in MODFLOW and is used here to simulate transport through the binary porous medium. A fluid is injected via a cross pattern of five wells within the single coarse-scale grid-block in the lower-left corner and extracted via a similar configuration of pumping wells on the top-right coarse grid-block to create a steady-state flow field. To calculate the breakthrough times, we reverse the steady-state velocity field. Then, for each coarse-scale sensor grid-block, we release 121 particles from a uniformly spaced $11 \times 11$ configuration of locations and advect those particles back to the injection wells using the reversed velocity field. The time it takes for half the particles (median of the distribution) released in a particular grid-block to reach the lower-left (injection) grid-block is taken

as the breakthrough time. Repeated for each of the sensor grid-blocks, we obtain the dynamic data $\mathbf{t}_b^{(obs)}$. Gaussian observation errors ($\sim \mathsf{N}(0, \{0.001\}^2)$, i.i.d.) are added to them after non-dimensionalization (non dimensional time = (raw time)*(injection rate)/(domain pore volume)). Thus the breakthrough times contain the effect of the fully resolved binary medium on the advective transport dynamics.

*4.2.3. The error model*

The error model in the inference accounts for both the measurement error and the model error. The error model for $\mathbf{k}^{(obs)}$ was obtained using offline runs. We sampled sets of $\{\mathbf{F}, \delta\}$ and developed a number of fine-scale realizations for each. We calculated their effective log-permeability using the method described above (using MODFLOW) for grid-blocks. A measurement error (same as mentioned in Sec. 4.2.2) was also added. The effective log-permeability of the realizations was also estimated using our upscaling model ($\mathcal{K}_e(\mathbf{F}, \delta)$). The discrepancy between the MODFLOW-upscaled effective log-permeability, and our upscaling model $\mathcal{K}_e(\mathbf{F}, \delta)$ was represented as a Gaussian distribution with mean $\boldsymbol{\mu}_k = 0.033$ and standard deviation $\sigma_k = 0.131$. The standard deviation for the breakthrough time, $\sigma_t$, is set to 5% of the maximum non-dimensional breakthrough time observed in the SSA set of sensors. These values are used in (9) and (12).

*4.2.4. The prior model*

Below, we summarize the prior beliefs employed in performing the inversion.

- We assume that the prior covariance for $\boldsymbol{\zeta}$ is close to the posterior i.e., we can use the Karhunen-Loève modes computed from the prior covariance to estimate the *posterior* $\boldsymbol{\zeta}$ distribution. The prior on the Karhunen-Loève weights is $w_i \sim \mathsf{N}(0, 1)$.

- We sample from (12) using the log form of $\delta$, i.e. $\ln(\delta)$. We model its prior using a truncated Gaussian

$$\ln(\delta) \sim \mathsf{N}(\ln(10), 2^2) \text{ if } 1 < \delta < 100.$$

  Outside these limits, the prior is set to zero, thus loosely modeling the inclusions to be larger than a fine-scale grid-cell, but smaller than a (coarse) grid-block.

- 30 terms were retained in the Karhunen-Loève expansion of the spatial field i.e., $M = 30$ in (10). We computed the energy captured by 30 Karhunen-Loève modes using (4) and compared it with that captured by 300 modes. The 30 modes account for 95.5% of the energy.

*4.2.5. Generation of the posterior distribution $P(\mathbf{w}, \delta|\mathbf{d})$*

The inverse problem was solved by taking between one and five million samples from the posterior distribution (12). An adaptive Markov chain Monte Carlo sampler,

called the Delayed Rejection Adaptive Metropolis (DRAM, [54]) was used for this purpose. The chain was checked for mixing and burn-in using the metric in [67] (as implemented in the `mcgibbsit` package [68] in R [69]) by monitoring the $5^{th}$ and $95^{th}$ percentiles as well as the median. 10,000 samples were retained by thinning the chain and this sample set is used for developing posterior distributions of the objects of inference. We checked the impact of thinning by computing the percentiles with a chain thinned to 100,000 samples (instead of 10,000); no significant change was observed.

In Fig. 3 we plot the probability density functions (PDF) for $w_1, w_{15}, w_{30}$ and $\ln(\delta)$, by marginalizing over the thinned samples. The three weights, $w_1, w_{15}, w_{30}$, correspond to Karhunen-Loève modes which are representative of large, medium and small-scale (but resolved) structures. Their joint PDFs are also plotted. We see that the posterior distribution for $w_1, w_{15}$, and $w_{30}$ are roughly Gaussian, though that does not hold true for $\ln(\delta)$ (which is a truncated Gaussian). The median value of $\delta$ is found to be 5.16 grid-cells (compared to the true value of 11.774) with a 90% credibility interval of (1.25– 18.25) grid-cells. The interquartile range is (2.55–10.08) grid-cells. Thus $\delta$ is clearly underestimated and there is significant uncertainty in its estimate. The approximately Gaussian (posterior) distributions for $w_{15}$ and $w_{30}$ are centered around 1, unlike the priors which are standard normals (centered at 0.0). The scatter plots show that the samples of these four parameters are not correlated with each other; the correlations between the (posterior of the) weights of adjacent Karhunen-Loève modes weaken very quickly and are insignificant for modes which are at least 5 modes apart.

### *4.3. Results and discussion*

In this section, we analyze the solution of the inverse problem. We first perform the inversion using both the static and dynamic data, and then repeat using the static and dynamic data individually. These steps are done to explore the contribution of each type of data to the inference.

#### *4.3.1. Assessment of* $\mathbf{F}(\mathbf{x})$ *and* $\mathbf{K}_e(x)$ *inferences*

We use the samples from $P(\mathbf{w}, \delta|\mathbf{d})$ (12) to generate realizations of $\mathbf{F}_i(\mathbf{x})$ and $\mathbf{K}_{e,i}, i = 1 \ldots 10,000$. The first 500 samples are discarded as "burn-in". In Fig. 4, in the top row, we plot their expected values $\overline{\mathbf{F}} = \mathbb{E}[\mathbf{F}(\mathbf{x})]$ and $\overline{\mathbf{K}_e(x)} = \mathbb{E}[\mathbf{K}_e(x)]$ in color while the "true" values (as plotted in Fig. 1, middle row) are plotted as dotted contours. For $\overline{\mathbf{F}}$, we see that the shade plot and the contours are similar with respect to large scale structures, though there are differences at smaller scales. On the other hand, the $\overline{\mathbf{K}_e(x)}$ plot at the top right shows significant differences between the shade and contour plots. This arises mostly because of the sharp gradients in $\mathbf{K}_e(x)$ and the approximations inherent in the $\mathcal{L}(\mathbf{F}(\mathbf{x}), \delta)$ model for the log-permeability. In the middle row of Fig. 4, we plot the grid-block-wise standard deviation of the 9,500 samples of $\mathbf{F}_i(\mathbf{x})$ and $\mathbf{K}_{e,i}$, along with the locations of the sensors in SSA.

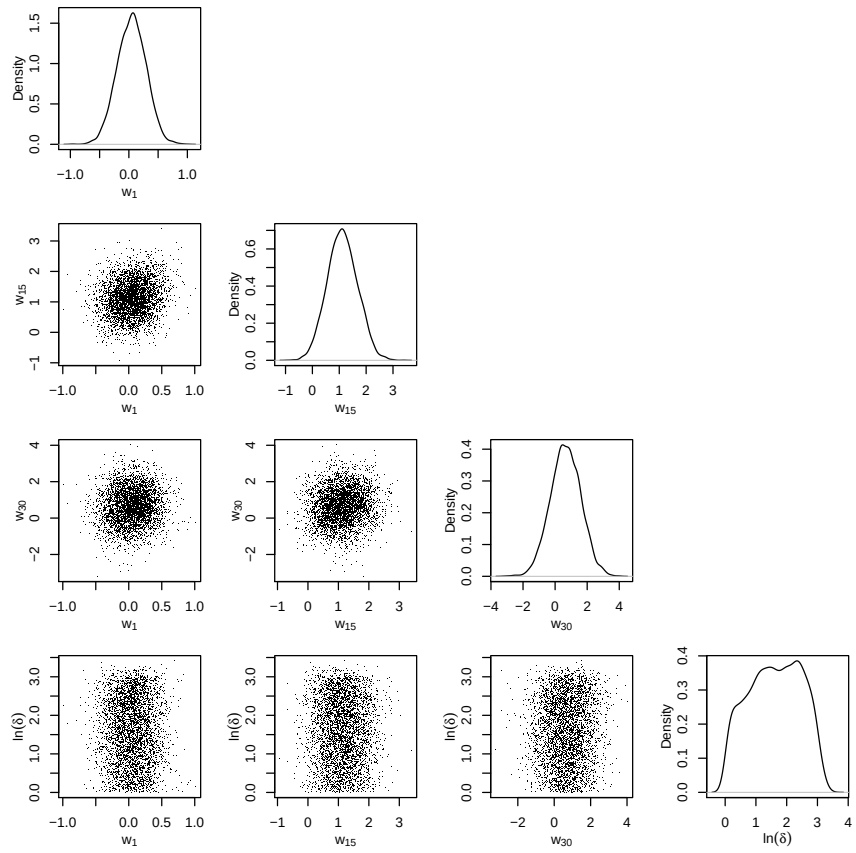


Figure 3: Plot of the joint and marginal probability densities of $w_1, w_{15}, w_{30}$ and $\ln(\delta)$ from the posterior distribution. The joint distributions show very little correlations between the Karhunen-Loève modes at the large, medium and small scales, as well as their correlations with $\delta$. Also, PDFs of the individual parameters are roughly Gaussian, with the exception of $\delta$.

Standard deviations (the uncertainty in the inferences) reach minimum values at the measurement points and increase in the poorly instrumented regions. The regions with the largest uncertainties are concentrated in regions of high gradients. The bottom row shows the difference between the true and average values i.e. $\epsilon_F = \mathbf{F}_c^t(\mathbf{x}) - \overline{\mathbf{F}}$ and $\epsilon_K = \mathbf{K}_c^t - \overline{\mathbf{K}_e(x)}$. Regions of low errors are generally at the sensor locations. In the plot for $\epsilon_K$, the largest errors correspond strongly with the "wall" of high gradients in $\mathbf{K}_e(x)$ near $x = 25$. The error approaches 50% in this region.

We repeat the experiment above using only the static data $\mathbf{k}^{(obs)}$ and plot the $\overline{\mathbf{F}} = \mathbb{E}[\mathbf{F}(\mathbf{x}))]$ and $\overline{\mathbf{K}_e(x)} = \mathbb{E}[\mathbf{K}_e(x)]$ in Fig. 5, top row. Again, 9,500 samples are used. Comparing the shade plot with the true field (plotted as contours), we see that the inversion captures the large structures but not the smaller details. Their equivalents, obtained from inversions that used only the dynamic data $\mathbf{t}_b^{(obs)}$ are plotted in Fig. 5,

bottom row; they bear little resemblance to the true field. We omit the standard deviations, $\epsilon_F$ and $\epsilon_K$ for both the cases, but they may be found in [70]. The standard deviation for the static-data-only inversion shows much the same behavior as in Fig. 4, i.e., they are minimum at sensor points.

*4.3.2. Assessment of* $\{\mathbf{w}, \delta\}$ *inferences*

The marginalized PDFs for $w_1, w_{15}, w_{30}$ and $\ln(\delta)$ for all three combinations of conditioning data are shown in Fig. 6. We also plot the prior distributions (using symbols) for comparison. The top left figure shows that the observations are most informative about $w_1$ (i.e., the difference between the prior and posterior is the largest), the Karhunen-Loève mode corresponding to the largest structures. The grid spacing of the sensors in SSA is smaller than the length-scale of the first Karhunen-Loève mode and provides dense sampling of it. Consequently, the distribution of $w_1$ obtained using just the static data is almost identical to that obtained from using both static and dynamic data. Relative to the static data, the dynamic data contributes very little to the inference of the lower (larger scale) Karhunen-Loève modes - the posterior for $w_1$ in Fig 6 (top left) is barely different from the prior. For intermediate Karhunen-Loève modes e.g., $w_{15}$, (top right in Fig. 6) both the static and dynamic data contribute to the inference, though the contribution of the static data is larger; the posterior developed from static data alone is quite close that developed using $\{\mathbf{k}^{(obs)}, \mathbf{t}_b^{(obs)}\}$. At the small scales i.e., $w_{30}$ (Fig. 6, bottom left), the dynamic data contributes little - the posterior distributions obtained from the $\mathbf{k}^{(obs)}$-only and $\mathbf{t}_b^{(obs)}$-only inversions are almost the same as the prior, whereas the inversion conditioned jointly on $(\mathbf{k}^{(obs)}, \mathbf{t}_b^{(obs)})$ is somewhat informative. Thus, dynamic data is informative, *only after* the larger/coarser scales have been accounted for by the static data; by itself, $\mathbf{t}_b^{(obs)}$ does not have the information content to resolve both scales. Transport occurs preferentially through high permeability regions, which can be affected by the smallest scales; since breakthrough times are the integrated effect of the travel times of the tracer, one may naively expect that the effect of small scale variations are easily captured there. However, breakthrough times are also affected by the larger Karhunen-Loève modes and deconvolving the impact of the smaller and larger lengthscales cannot be done without $\mathbf{k}^{(obs)}$, which uniquely capture the coarse-scale structures. The inference using SSA sensors develops the distribution for $\delta$ almost entirely based on $\mathbf{k}^{(obs)}$; adding $\mathbf{t}_b^{(obs)}$ modifies the distribution only modestly. Inversions using just $\{\mathbf{t}_b^{(obs)}\}$ results in a posterior distribution for $\delta$ indistinguishable from the prior. Also, as discussed in Sec. 4.2.5, $\delta$ is underestimated.

*4.3.3. Impact of the number of sensors*

In Fig. 7 we compare the marginalized posteriors for $w_1, w_{15}, w_{30}$ and $\ln(\delta)$ as obtained with sensor-sets SSA and SSB. Both static and dynamic data were used in the estimation. The second set, which has more than half as many sensors, results in a PDF for $w_1$ which is sharper than that obtained with SSA, while the PDF for

$\ln(\delta)$ is almost unchanged and not very different from the prior. Also, the PDFs for $w_{15}$ and $w_{30}$ change significantly when recomputed using SSB, indicating that the information content of $\mathbf{t}_b^{(obs)}$ with respect to finer scale structures collected by SSA and SSB could be different; the marginals developed using the SSB sensor set are steeper.

In order to analyze the model fits arising from SSA and SSB measurements, we conduct a posterior predictive check using $\mathbf{t}_b^{(obs)}$. Note that since inferences were drawn using both $\mathbf{k}^{(obs)}$ and $\mathbf{t}_b^{(obs)}$, good fits with $\mathbf{k}^{(obs)}$ may compensate for bad fits with $\mathbf{t}_b^{(obs)}$. In Fig. 8, we plot the results of posterior predictive check performed using inferences drawn from both SSA and SSB. We use the realizations $\mathbf{F}_i(\mathbf{x}), i = 500 \ldots 10,000$, to generate the corresponding coarse-scale $\mathbf{K}_{e,i} = \mathcal{L}(\mathbf{F}_i(\mathbf{x}), \delta_i, \kappa)$; thereafter $\mathbf{t}_{b,i} = \mathcal{M}(\mathbf{K}_{e,i})$ at the SSA- and SSB-sets of sensors. We plot the median, the $1^{st}$ and the $99^{th}$ percentile of the breakthrough times. The spread of the replicates of $\mathbf{t}_b$ obtained with SSB (right figure) is generally smaller than those obtained with SSA, indicating a reduction in predictive uncertainty.

We next evaluate the predictive ensemble of breakthrough times (plotted for SSA and SSB in Fig. 8) quantitatively using the continuous rank probability score (CRPS), the mean absolute error (MAE) and the interval score (IS) [71, 72]. These metrics are defined for each sensor / observation; we report metrics averaged over all sensors (in SSA or SSB). 950 samples from the predictive ensemble (rather than the full 9500 ensemble members) were used for the purpose; the sensitivity of the metrics to the number of samples was checked by repeating the calculations with double and half the number of samples. The interquartile range was used for calculating the IS. In Table 1, we tabulate the CRPS, MAE and IS for the two predictive ensembles in Fig. 8. Results indicate that predictions at the SSB sensors are slightly more accurate (i.e., similar to observations) and produce a more predictive ensemble, Fig. 8 (right).

| Ensemble | CRPS | MAE | IS |
|---|---|---|---|
| SSA | 0.038 | 0.052 | 0.167 |
| SSB | 0.040 | 0.051 | 0.160 |

Table 1: CRPS, MAE, and IS for the predictive ensembles of breakthrough times developed from the SSA and SSB sensor sets (see Fig. 8). CRPS, MAE and IS have units of breakthrough times i.e., they are non-dimensional. The metrics show that the inversion performed using the SSB sensors leads to a slightly more predictive model.

Finally, we address the question of whether the change in the posterior density of $w_{15}$ and $w_{30}$ in Fig. 6, when the inference is conducted using $\{\mathbf{k}^{(obs)}, \mathbf{t}_b^{(obs)}\}$ (vis-à-vis the estimation using just $\{\mathbf{k}^{(obs)}\}$), is due to the larger number of observations that are used in the former or due to the different *types* of information in $\mathbf{k}^{(obs)}$ and $\mathbf{t}_b^{(obs)}$. In Fig. 9, we plot the posterior densities of $w_{15}$ and $w_{30}$ as obtained using the SSA

and SSB sets of sensors, computed using just $\{\mathbf{k}^{(obs)}\}$ observations (i.e., static-data only) as well as conditioned jointly on $\{\mathbf{k}^{(obs)}, \mathbf{t}_b^{(obs)}\}$ (i.e., static and dynamic data). If the difference in the estimation of $w_{15}$ using $\{\mathbf{k}^{(obs)}, \mathbf{t}_b^{(obs)}\}$ versus $\{\mathbf{k}^{(obs)}\}$ (both obtained from SSA sensors) had been due to the number of observations ($\{\mathbf{k}^{(obs)}, \mathbf{t}_b^{(obs)}\}$ has 20 observations of each type), then the posterior distribution computed using just the static data obtained from the SSB sensor set (34 observations) should be similar to that computed from the 40 $\{\mathbf{k}^{(obs)}, \mathbf{t}_b^{(obs)}\}$ observations from the SSA set (20 observations each of$\{\mathbf{k}^{(obs)}\}$ and $\{\mathbf{t}_b^{(obs)}\}$). However, Fig. 9 (left) shows quite the opposite trend, as the posterior computed from just the static data from the SSB sensors set *moves away* from that computed using $\{\mathbf{k}^{(obs)}, \mathbf{t}_b^{(obs)}\}$ from the SSA sensor set. Further, since the larger number of observations in SSB resolve $w_{15}$ better (vis-à-vis SSA), the static-data only estimate of $w_{15}$ is quite close to the posterior obtained from using both $\{\mathbf{k}^{(obs)}, \mathbf{t}_b^{(obs)}\}$ from the SSB sensors. Thus, the difference in the posterior distributions is not due to the extra observations in $\{\mathbf{k}^{(obs)}, \mathbf{t}_b^{(obs)}\}$; rather it is due to the different *types* of information in $\{\mathbf{k}^{(obs)}\}$ and $\{\mathbf{t}_b^{(obs)}\}$. In Fig. 9 (right), we see that the posterior densities of $w_{30}$ obtained from the SSA and SSB sensors using just the static data are rather similar to each other and to the prior. This is because neither of the two sensor sets are dense enough to resolve $w_{30}$. However, when $\mathbf{t}_b^{(obs)}$ are used in the inference, the posterior densities differ from those obtained using just the static data, particularly for the SSB sensors. Furthermore, we do not see a trend; had the posterior distribution of $w_{30}$ been solely dependent on the number of observations, the static-only estimate from SSB should have occupied a position between the static-only estimate of $w_{30}$ drawn from SSA sensor set and the SSA estimate conditioned on $\{\mathbf{k}^{(obs)}, \mathbf{t}_b^{(obs)}\}$. Clearly, this is not the case in Fig. 9 (right).

### *4.4. Summary*

To summarize, we have developed an inference scheme, predicated on a multiscale link function, to infer coarse-scale features and summaries of fine-scale structures of a random binary field from a combination of static and dynamic observations. We can estimate a spatially variable proportion $\mathbf{F}(\mathbf{x})$ of the high-permeability material from observations that are obtained on the coarse-scale but are nevertheless informative about the fine-scale. The size of the inclusions, $\delta$, is under-estimated and there is significant uncertainty in the estimate. This arises from the behavior of the link function $\mathcal{L}$. As seen in Fig. 2 (left), the link function generally underestimates the effective permeability; further, as seen in Fig. 2 (right), smaller $\delta$ lead to larger $\mathbf{K}_e$ when $\mathbf{F} < 0.5$. Thus when $\mathcal{L}$ is used to fit to data, it compensates for its tendency to underestimate effective permeability by indicating a smaller $\delta$. Further, $\mathbf{K}_e$ is sensitive to $\delta$ approximately in the region $0.3 \leq \mathbf{F} \leq 0.7$ for small $\delta/\Delta$; thus, since only a few grid-blocks lie in this sensitive range, $\delta$ can only be estimated with large uncertainty. Computational experiments with fields where $\mathbf{F}(\mathbf{x})$ restricted around 0.5 e.g., $0.4 < \mathbf{F}(\mathbf{x}) < 0.6$, have shown that $\delta$ can be inferred quite accurately [73].

We see that the static data can inform on the large-scale features mainly because the distribution of sensors is sufficient to resolve such structures. The dynamic data, which is an integrated measure of the effect of small variations in the permeability field is key to estimating smaller (but nevertheless resolved) structures. Increasing the number of sensors leads to estimates with lower uncertainties.

We have also explored how the static ($\mathbf{k}^{(obs)}$) and dynamic ($\mathbf{t}_b^{(obs)}$) data contribute to the estimation of $\{\mathbf{w}, \ln(\delta)\}$. By itself, $\mathbf{t}_b^{(obs)}$ is not sufficiently informative to estimate both the large-scale structures and the smaller details. However, if the large-scale structures are constrained/estimated using $\mathbf{k}^{(obs)}$, the smaller details can be inferred from $\mathbf{t}_b^{(obs)}$. Thus joint inversions on $\{\mathbf{k}^{(obs)}, \mathbf{t}_b^{(obs)}\}$ result in more accurate estimations of $\{\mathbf{w}, \ln(\delta)\}$ not only because of the larger number of observations involved, but rather because of the *type* of information. Since $\mathbf{k}^{(obs)}$ is informative about the larger length scales in the domain while $\mathbf{t}_b^{(obs)}$ is impacted most by the smaller scales that contort the flowpaths in the porous medium, joint inversion conditions the estimates to *multiscale* data.

In the next section (Sec. 5), we explore the robustness of the inference. Since the aim of reconstructing a permeability field is generally to use it to predict transport phenomena, we will subject the reconstructions conditioned on multiscale data (as well as those obtained individually from static and dynamic data) to posterior predictive tests involving transport on ensembles of fine-scale binary fields.

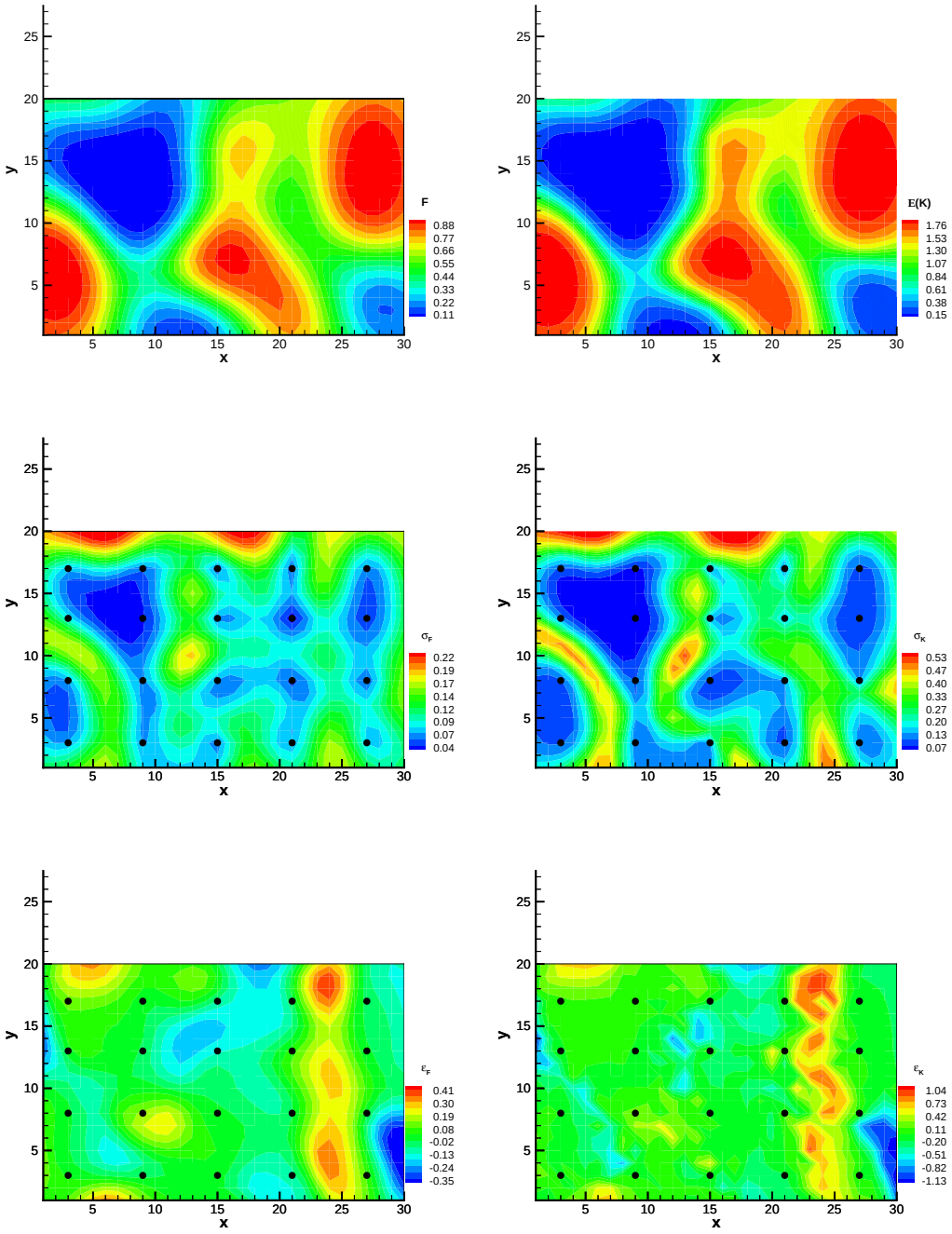


Figure 4: Results from the inference, computed using 9500 samples from the posterior distribution. In the top row, we plot the means $\overline{\mathbf{F}} = \mathbb{E}[\mathbf{F}(\mathbf{x})]$ and $\overline{\mathbf{K}_e(x)} = \mathbb{E}[\mathbf{K}_e(x)]$; they bear a strong resemblance to the true values in Fig. 1 (middle row) and also plotted as overlaid contours. In the middle row, we plot the pointwise standard deviation of $\mathbf{F}_i(\mathbf{x})$ and $\mathbf{K}_{e,i}$; they are smallest at the sensor locations. In the bottom row, we plot the errors $\epsilon_F = \mathbf{F}_c^t(\mathbf{x}) - \overline{\mathbf{F}}$ and $\epsilon_K = \mathbf{K}_c^t - \overline{\mathbf{K}_e(x)}$, which show large values in regions of high gradients.

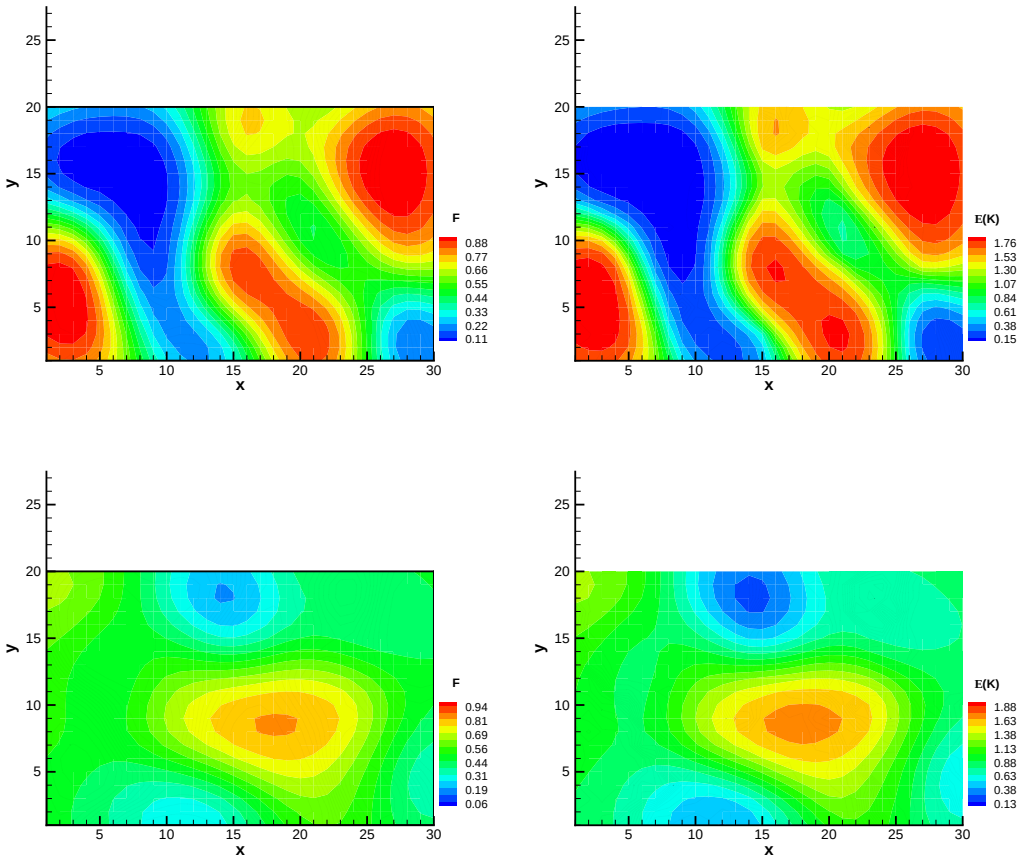


Figure 5: Top: Results (the means $\overline{\mathbf{F}}$ and $\overline{\mathbf{K}_e(x)}$) from an inversion using only static data. The true values are plotted as contours. Bottom: Their counterparts, calculated using only dynamic data. Computations were done using 9,500 samples as in Fig. 4. We see that the static-data-only inversion in the top row are slightly worse than the results in Fig. 4; they miss the finer details and are overly smooth. The inversions in the bottom row bear little resemblance to the true $\mathbf{F}_c^t(\mathbf{x})$ and $\mathbf{K}_c^t$ plotted as contours.

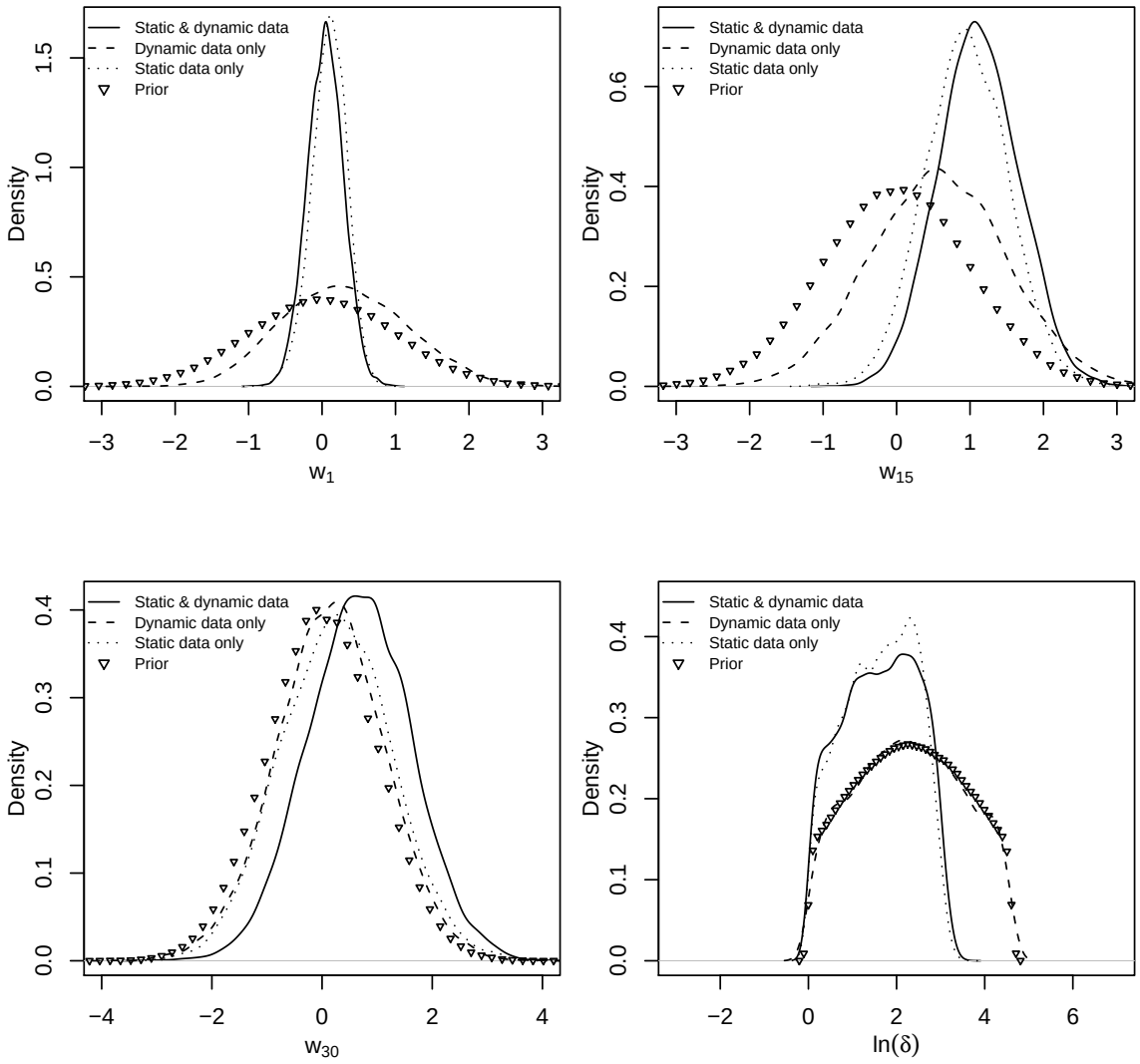


Figure 6: Marginalized PDFs of $w_1, w_{15}, w_{30}$ and $\ln(\delta)$ as inferred from $\mathbf{k}^{(obs)}$-only (dotted lines), $\mathbf{t}_b^{(obs)}$-only (dashed lines) and jointly from $(\mathbf{k}^{(obs)}, \mathbf{t}_b^{(obs)})$ (solid lines). The priors are plotted with $\nabla$ for comparison. Note that the prior and posterior densities for $\ln(\delta)$, plotted in the bottom right figure are truncated at $\ln(\delta) = 0, 4.6$ but the kernel density estimates used to create plots smooth them near the truncation limits.

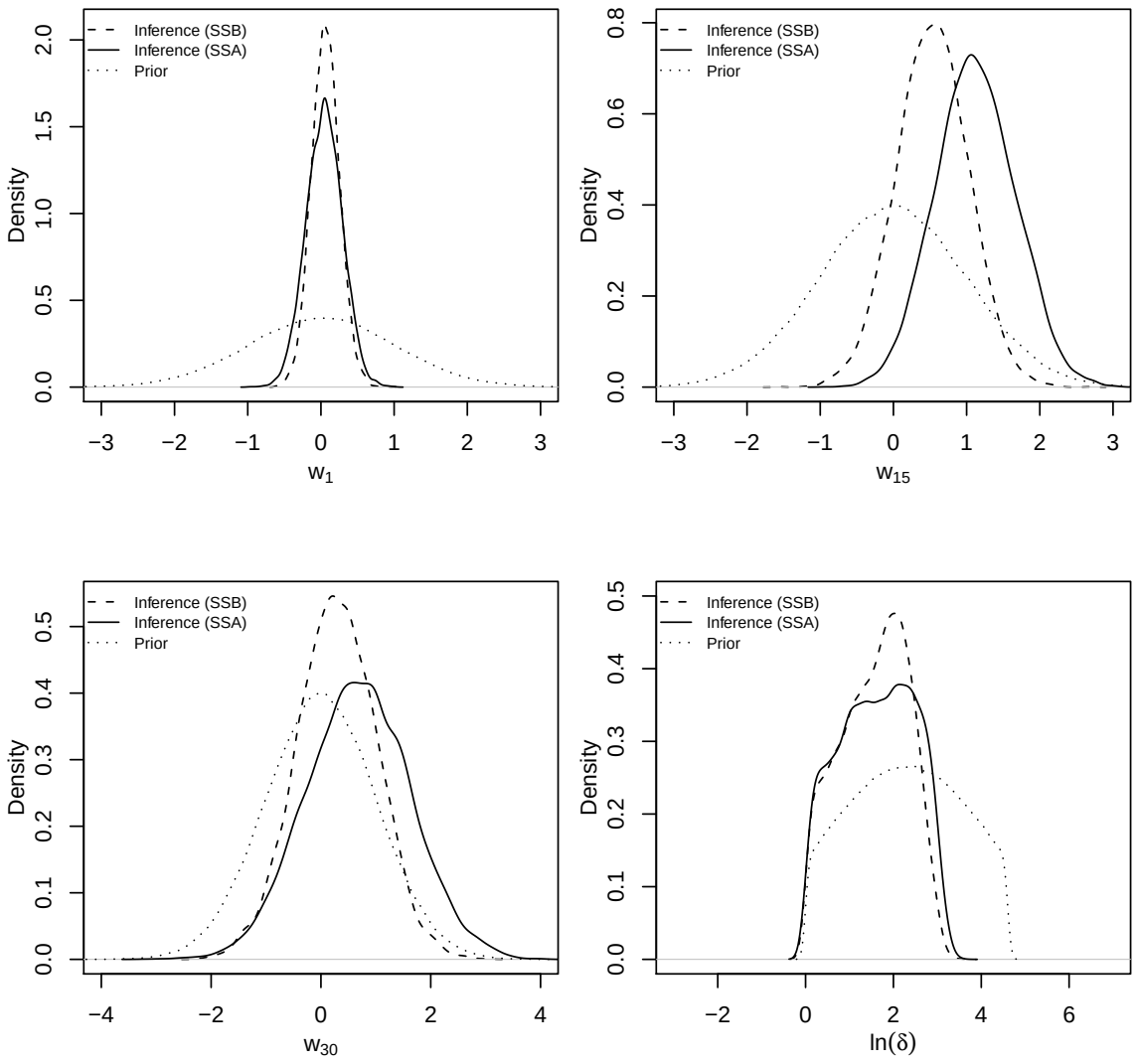


Figure 7: Prior and marginalized posterior values of the Karhunen-Loève mode weights $w_1, w_{15}, w_{30}$ and $\ln(\delta)$ as computed using the sensor-sets SSA (solid line) and SSB (dashed line). We see that the posteriors for $w_1$ are similar, indicating that the higher sensor density of SSB collects little extra information on them. However, the PDFs for $w_{15}$ and $w_{30}$ are quite different, indicating that the uncertainty in their values may have been underestimated in both cases. The posterior density for $\ln(\delta)$ (bottom right) obtained from either set of sensors is not very different from the priors.

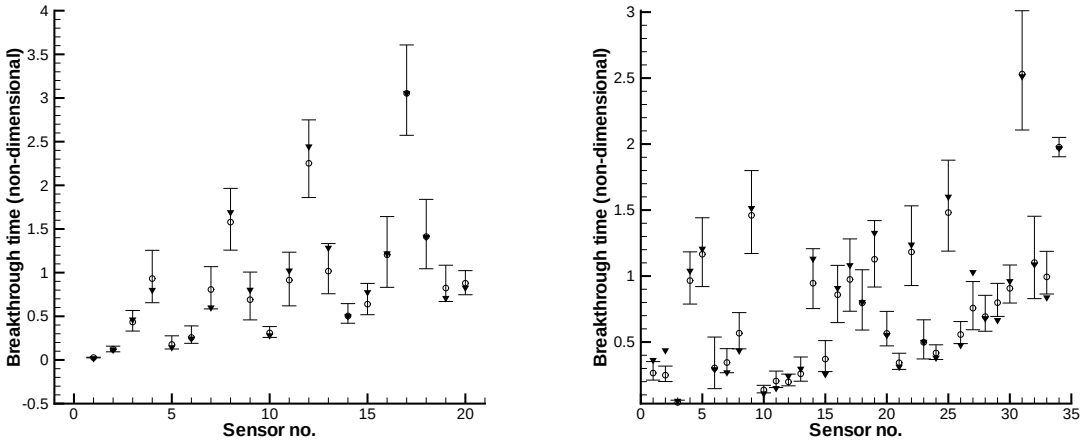


Figure 8: Results from the posterior predictive check for breakthrough times conducted by generating coarse-scale $\mathbf{K}_{e,i}$ and using $\mathcal{M}(\mathbf{K})$ to generate the breakthrough times. The filled, inverted triangles are the observations at the sensors. The median breakthrough times from the posterior predictive checks are plotted with open symbols and the error bars denote the $1^{st}$ and $99^{th}$ percentiles of the breakthrough time distribution. Results for SSA observations (Left) and SSB observations (Right).

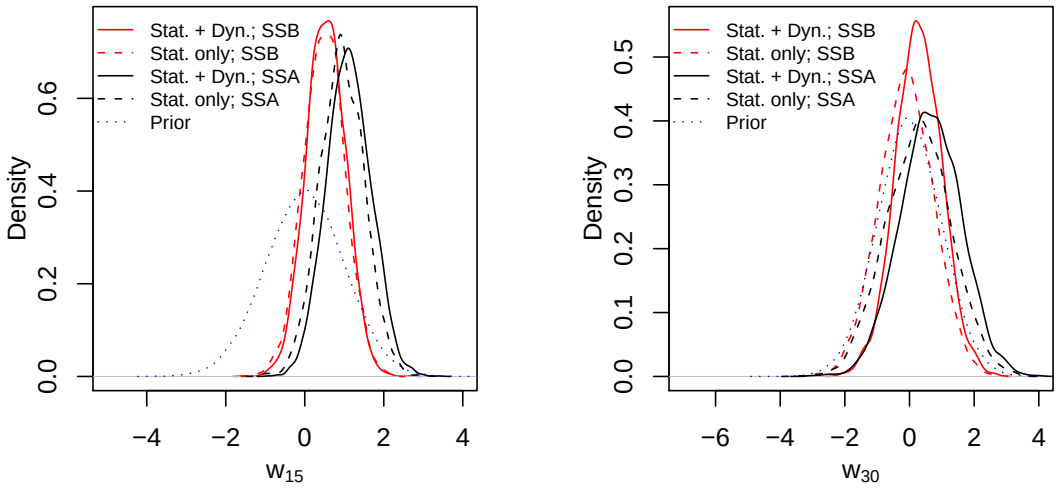


Figure 9: Posterior densities of $w_{15}$ and $w_{30}$ obtained using just the static observations $\mathbf{k}^{(obs)}$ (dashed lines) as well as static and dynamic data $\{\mathbf{k}^{(obs)}, \mathbf{t}_b^{(obs)}\}$ (solid lines). The priors are plotted with dots. Estimates drawn from SSA sensors are in black; their SSB counterparts are in red. Left: The $w_{15}$ density drawn solely from SSB $\mathbf{k}^{(obs)}$ (34 observations) is quite different from the density obtained from SSA observations (of any type). Instead, it shows a marked similarity to the posterior distribution obtained from SSB $\{\mathbf{k}^{(obs)}, \mathbf{t}_b^{(obs)}\}$. Right: The $w_{30}$ distributions obtained from static data only are very similar to the prior, regardless of the sensor set; the distribution becomes informative (different from the prior) only when $\mathbf{t}_b^{(obs)}$ are included. Thus, it is the *type* of data, rather than the quantity, that renders the posterior densities informative.

## 5. Posterior predictive modeling

The discussion in Sec. 4 focused on the probabilistic reconstruction of inclusion proportion $\mathbf{F}(\mathbf{x})$ and a lengthscale $\delta$ on a coarse $30 \times 20$ mesh. However, the link function $\mathcal{L}$ allows us to also construct realizations of the fine-scale binary medium, given $\{\mathbf{w}, \delta\}$. In this section, we explore the difference between fine-scale binary permeability fields developed by conditioning $P(\mathbf{w}, \delta|\mathbf{d})$ jointly on static and dynamic data (multiscale data) and those reconstructed from only one type of data. We assess them based on their ability to reproduce the observed breakthrough times at the SSA sensors. $P(\mathbf{w}, \delta|\mathbf{d})$ is used to develop realizations of the *fine-scale* binary medium (on a $3000 \times 2000$ mesh) as outlined in Sec. 4.2, which is then incorporated in flow simulations using MODFLOW and advective transport using MODPATH.

Fig. 10 shows example realizations of the binary medium which are consistent with the multiscale observations i.e., they were developed from $\{\mathbf{w}, \delta\}$ conditioned on $\{\mathbf{k}^{(obs)}, \mathbf{t}_b^{(obs)}\}$. The white and gray regions are the high and low permeability phases, respectively. A single particle track from the injection wells to each of the SSA sensors is also shown. We choose eight $\{\mathbf{w}, \delta\}_i$ samples from the posterior to develop the corresponding $\mathbf{F}_i(\mathbf{x})$ from (11). Then, using the procedure (based on excursion sets of multiGaussian [mG] fields) described in Sec. 3.3, we develop the corresponding fine-scale binary field on a $3000 \times 2000$ mesh. The true binary field is plotted in the middle of the figure (Fig. 10(e)). The variation between realizations is due to both the stochastic nature of the construction process, where white noise is convolved with a Gaussian kernel, and the sampled value of $\delta$, which is different for each realization. Of these eight examples, realization (g) has the largest $\delta$ value and realization (i) has the smallest.

Three combinations of $\mathbf{k}^{(obs)}$ and $\mathbf{t}_b^{(obs)}$ conditioning data ($\{\mathbf{k}^{(obs)}, \mathbf{t}_b^{(obs)}\}, \{\mathbf{k}^{(obs)}\}, \{\mathbf{t}_b^{(obs)}\}$) were used, and for each combination, 1000 fine-scale binary realizations were created. For each of the SSA sensors and for each realization, the median travel time between the injector and the sensor is determined. Recall that sensor locations are defined at the grid-block scale and that for each location a total of 121 particles are tracked between the injector and the sensor. The median time from these 121 particles is extracted at each sensor location and designated as the breakthrough time for that location. A distribution of breakthrough times across the 1000 realizations is then created. Fig. 11 (left) shows a comparison of the three breakthrough time CDFs (cumulative distribution function) against the observed breakthrough time for sensor location 14 (coordinates: 21,13). All three distributions capture the observed breakthrough time (accurate) with the "Fine and Coarse" (alternatively, inferred jointly from $\{\mathbf{k}^{(obs)}, \mathbf{t}_b^{(obs)}\}$) and "Fine Only" data (alternatively, inferred solely from $\{\mathbf{t}_b^{(obs)}\}$) combinations being the narrowest (most precise) although somewhat biased towards underestimation of the observed travel time. The "Coarse Only" data combination (alternatively, inferred solely from $\{\mathbf{k}^{(obs)}\}$) produces a breakthrough time distribution that is less precise but also less biased.

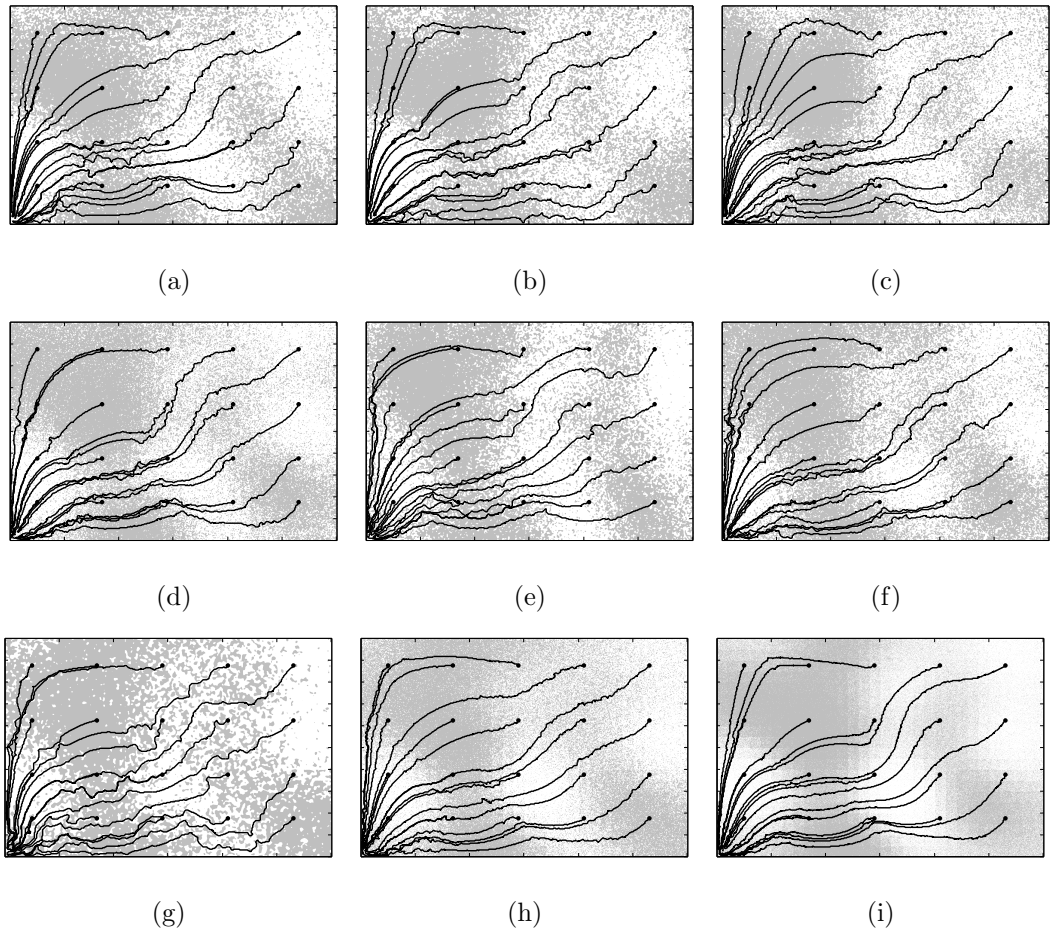


Figure 10: Fine-scale realizations of the random binary field conditioned on the observations and showing a single flowpath from the injection wells to each SSA sensor. These were developed from the posterior distribution of $\{\mathbf{w}, \delta\}$ using the mG-based technique described in Sec. 3.3. The center image (e) is the ground truth fine-scale realization. White indicates high permeability and gray is low permeability. Variation in the binary patterns are due to the stochastic nature of the process and the variation in the estimated $\delta$ parameter between realizations.

Fig. 11 (right) shows the precision and bias for all 20 SSA sensors and provides perspective on how these quantities change across the model domain. For each sensor location, the black "+" indicates both the location of the sensor and the relative location of the observed breakthrough time. The distribution of breakthrough times from each combination of $\mathbf{k}^{(obs)}$ and $\mathbf{t}_b^{(obs)}$ is shown as a circle. The center of the circle is offset from the observed breakthrough time by the amount of bias, calculated here as the difference between the median of the distribution and the observed value. Underestimation shifts the center of the circle to the left and over estimation to the right. The center 95% of the breakthrough time distribution defines the radius of the circle. Both the radius and the bias offset are calculated in units of dimensionless travel time. The axes scales in Fig. 11 (right) serve as both geographic coordinates and travel time measures to define both the sensor locations and the relationship of the median breakthrough time distributions to the observed breakthrough time. At each location, the order of the circles is set such that the smallest (tightest distribution) is at the front and the largest is at the back.

Examination of Fig. 11 (right) shows that all three combinations of $\mathbf{k}^{(obs)}$ and $\mathbf{t}_b^{(obs)}$ create accurate distributions of breakthrough times (all circles contain the observed value denoted by the "+"). Additionally, estimated fields that are conditioned jointly on $\{\mathbf{k}^{(obs)}, \mathbf{t}_b^{(obs)}\}$ create the most precise distribution (black circle is smallest and therefore on the top) for the majority of the SSA locations. Bias is relatively small at all locations as shown by all three circles being approximately centered on the observed value. The spatial pattern shown Fig. 11 (right) is consistent with the flow patterns for this domain with a source and sink in the lower left and upper right corners. The breakthrough time distributions are most precise along the diagonal between the injector and producer where the majority of the flow takes place and least precise along the upper and lower boundaries where the flow fraction is quite low (see Fig. 1, b). The amount of bias is also smallest along the diagonal and greatest along the top and bottom boundaries. For additional details see [70].

Fig. 11 is focused on comparison of the probabilistic estimates of the breakthrough time to the observed values at the SSA sensor locations. However, since the ground truth in this study is known, it is possible to examine the quality of the travel time estimates for every location in the model domain. Fig. 12 (left) shows distributions of the average absolute error (AAE) between the estimated and true breakthrough time. Each average is calculated over all 600 coarse-scale grid blocks for a single realization and the distribution of the averages is then determined across all 1000 realizations. Lower values in the distribution come from realizations that better fit the true breakthrough time at all locations. The majority of the fields conditioned jointly to the $\{\mathbf{k}^{(obs)}, \mathbf{t}_b^{(obs)}\}$ or just the $\mathbf{k}^{(obs)}$ data have a median travel time AAE of less than 0.5 time units (Figure 12). Those fields conditioned to only $\mathbf{t}_b^{(obs)}$ data have considerably larger AAE values, up to 2.0 time units).

All comparisons shown above consider the breakthrough time values from the injector to one or more coarse grid cells. These comparisons are consistent with the

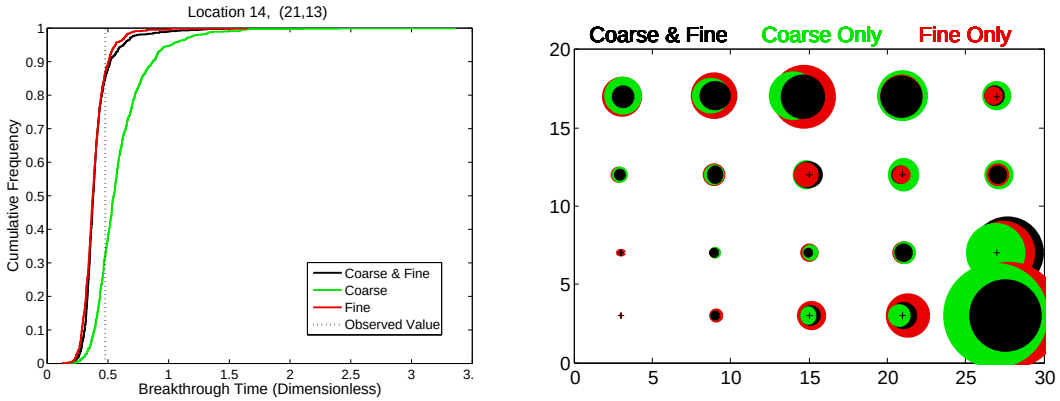


Figure 11: Comparison of the median travel times to the SSA sensors for three different data combinations. Left: Breakthrough time CDFs for 1000 samples are shown for an example location (sensor 14). Right: The circle plots summarize the breakthrough time distributions and compare them to the true breakthrough times for all sensor locations. Details are in the text. "Coarse & fine" refer to realizations conditioned jointly on $\{\mathbf{k}^{(obs)}, \mathbf{t}_b^{(obs)}\}$, "Coarse only" refer to inferences using on $\{\mathbf{k}^{(obs)}\}$ while "Fine only" indicates inferences conditioned only on $\{\mathbf{t}_b^{(obs)}\}$.

conditioning data, $\mathbf{t}_b^{(obs)}$ (median travel time), used in the inverse estimates. However, additional information can be gained from the full distribution of travel times to each coarse grid block. The two-sample Kolmogorov-Smirnov (KS) test is used to compare the true travel time distribution to the distribution calculated on each estimated field for each coarse-scale grid block. The KS test is a non-parametric test of the difference between two distributions. The KS test statistic is the maximum vertical distance, $D$ between two CDFs:

$$D_{i,j} = \sup_x |F_{i,n}(x) - F_{j,n'}(x)| \tag{13}$$

Here the $i^{\text{th}}$ and $j^{\text{th}}$ distributions have the same number of travel times, 121, for all comparisons ($n = n'$). Values of the $D$ statistic range from 0, when there is no difference between the distributions, to 1.0 when the values of distributions do not overlap at all. The null hypothesis of the KS test is that both samples come from the same underlying population. Here, for each fine-scale realization, we compare the modeled and observed travel time distribution at every location within the model domain and calculate the test statistic, $D$. The average value of $D$ across all 600 locations is retained for each of the 1000 realizations.

Fig. 12 (right) shows the resulting distributions of the average $D$ value for these sets of 1000 realizations. The smallest values of $D$ occur when both $\mathbf{k}^{(obs)}$ and $\mathbf{t}_b^{(obs)}$ are used as conditioning data. The distributions of $D$ when only $\mathbf{k}^{(obs)}$ or $\mathbf{t}_b^{(obs)}$ are

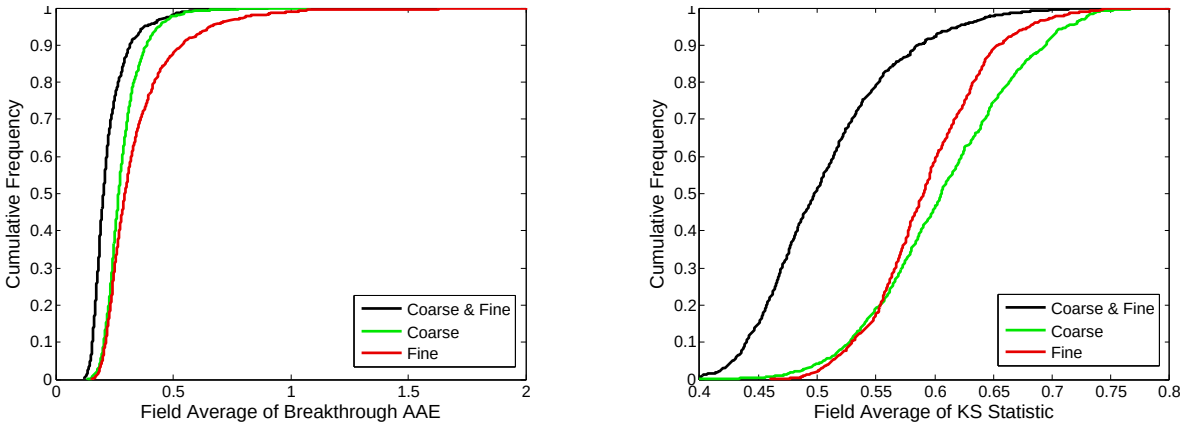


Figure 12: Average absolute errors (AAE) between median travel times from the estimated and true travel time distributions for all locations in each field (left) and distribution of average KS statistic values calculated by comparing the full distribution of estimated and true travel time distributions at all locations (right).

used have slightly larger values and are very similar.

To summarize, we sampled the distribution $P(\mathbf{w}, \delta|\mathbf{d})$, developed in Sec. 4.3, to construct 1000 realizations of the fine-scale binary medium on a $3000 \times 2000$ mesh and predict breakthrough times at the SSA sensors via simulation. This was performed for the three different $P(\mathbf{w}, \delta|\mathbf{d})$ developed (conditioned on $\{\mathbf{k}^{(obs)}, \mathbf{t}_b^{(obs)}\}$, $\{\mathbf{k}^{(obs)}\}$ and $\{\mathbf{t}_b^{(obs)}\}$) in Sec. 4.3 to gauge the impact of multiscale data in the estimation of $\mathbf{K}_e(x)$. Posterior predictive model evaluations using 1000 realizations created from each of the three combinations of conditioning data clearly showed that while all data combinations produce accurate results, using data collected on both scales i.e., $\{\mathbf{k}^{(obs)}, \mathbf{t}_b^{(obs)}\}$, as opposed to a single scale ($\{\mathbf{k}^{(obs)}\}$ or $\{\mathbf{t}_b^{(obs)}\}$), creates predictions that are most precise and closest to the observed values.

## 6. Conclusions

We have developed a multiscale, statistical technique to reconstruct characteristics of a random, porous binary medium from partial observations. The binary medium consists of high and low permeability material in spatially varying proportions. The geometry of the medium consists of inclusions of the less abundant material embedded in a matrix of the other. The uneven spatial distribution of the two materials, $\mathbf{F}(\mathbf{x})$, and a characteristic inclusion lengthscale, $\delta$, are the objects of inference. The inclusions are too small to be resolved on the coarse mesh and the effective permeability of a grid-block is $\mathbf{K}_e(x)$ is calculated using a deterministic upscaling model, i.e., $\mathbf{K}_e(x) = \mathcal{L}(\mathbf{F}(\mathbf{x}), \delta, \kappa)$. The observations consist of measurements of log-permeability

($\mathbf{k}^{(obs)}$) and breakthrough times ($\mathbf{t}_b^{(obs)}$) of a tracer from a tracer test at a set of sensor points. The log-permeability measurements inform on the large-scale variations in the domain of interest; the breakthrough times are governed strongly by the flow paths through the medium and are informative on the small-scale structures.

The reconstruction is posed as a Bayesian inverse problem, predicated on fitting a transport model to the data. The transport model is formulated at the coarse-scale, but with a statistical subgrid model that incorporates the impact of the fine, unresolved scales. The subgrid model (alternatively, the *link* function between the scales) is parameterized with the high-permeability material proportion, $\mathbf{F}(\mathbf{x})$, and characteristic length, $\delta$. The inverse problem is regularized by expressing $\mathbf{F}(\mathbf{x})$ using Gaussian processes; its dimensionality is reduced by expanding $\mathbf{F}(\mathbf{x})$ in terms of a truncated Karhunen-Loève series. Fitting the model to data yields a joint distribution of the Karhunen-Loève weights, inferring characteristics of the variation of $\mathbf{F}(\mathbf{x})$ and $\mathbf{K}_e(x)$ in the domain. This distribution is realized without any approximations, using an adaptive MCMC sampler.

We find that $\mathbf{F}(\mathbf{x})$ obtained by jointly conditioning on $\{\mathbf{k}^{(obs)}, \mathbf{t}_b^{(obs)}\}$ is far more accurate than if it is obtained solely from $\mathbf{k}^{(obs)}$ or $\mathbf{t}_b^{(obs)}$. Inversion based on $\mathbf{k}^{(obs)}$ captures the large-scale variation correctly; however, the permeability field distribution so reconstructed predicts breakthrough times poorly since it lacks smaller details/structures responsible for contorted flow paths. The inversions based solely on $\mathbf{t}_b^{(obs)}$ are extremely poor, due to inability of these data to constrain large structures. However, when the two are put together, $\mathbf{k}^{(obs)}$ constrains the larger structures while $\mathbf{t}_b^{(obs)}$ is used to constrain the smaller ones. Thus the improved inferences (when conditioned jointly on $\mathbf{k}^{(obs)}$ and $\mathbf{t}_b^{(obs)}$) are not just due to more plentiful observations, but rather due to the different *types* of information in $\mathbf{k}^{(obs)}$ and $\mathbf{t}_b^{(obs)}$. Since the information is derived from different scales (large for $\mathbf{k}^{(obs)}$ and small for $\mathbf{t}_b^{(obs)}$), the inversion is fundamentally multiscale.

We found that we could estimate the inclusion size $\delta$, but with significant uncertainty. This is because when one of the two components of the binary medium dominates e.g. $\mathbf{F} < 0.3$ or $\mathbf{F} > 0.7$, the sensitivity of the effective permeability to $\delta$ is muted, especially if the inclusions are small compared to the grid-block. In our case, a large fraction of the grid-blocks had a preponderance of one phase or the other, leading to the large uncertainty in the estimate. Further, the $\delta$ was underestimated as a consequence of the behavior of the subgrid model $\mathcal{L}$.

Plots of marginalized posteriors of the objects of inference show that they are approximately Gaussian. While the priors used for them are Gaussian, the posterior shapes are surprising, given that both the fluid transport and the link function are strongly nonlinear.

We use the inferences of $\mathbf{F}(\mathbf{x})$ and $\delta$ to reconstruct realizations of the resolved binary medium on a fine mesh. We check the predictive skill of the ensemble of realizations by performing transport simulations with them, in an effort to recreate the

observations from which they were inferred. We find that fine-scale realization developed by conditioning jointly on $\{\mathbf{k}^{(obs)}, \mathbf{t}_b^{(obs)}\}$ (i.e., "multiscale" realizations) have a greater predictive skill that those inferred with one type of information. Preliminary results indicate that the inferences may also be more robust for predictive modeling in situations where the flow patterns are very different from those used in the estimation [70].

This work raises a few new questions. While we find that multiscale inversion leads to more robustness in inferences of binary media, the Bayesian technique is computationally expensive and will probably scale only to problems of modest size. Approximating the posterior distribution as a Gaussian opens up the possibility of employing scalable Ensemble Kalman Filtering techniques, which are currently being investigated. A second avenue of research lies in whether the fine-scale realizations constructed from the data can be used in an efficient manner for predictions; currently, ensemble predictions require many simulations on a fine (e.g., $3000 \times 2000$) mesh. While an embarrassingly parallel problem, it nevertheless consumes significant computing resources and often does not provide a timely solution. Finally, we consider whether the incorporation of model errors into the inversion process can be performed in a more accurate manner. We are currently exploring ways in which the model errors can be used to jointly infer the Karhunen-Loève weights, $\delta$ and a permeability field from the same observations. Preliminary results, obtained by incorporating upscaling errors (modeled using kernel density estimation) in the inversion process, are encouraging [70].

## 7. Acknowledgements

This work was funded by the Laboratory Directed Research and Development (LDRD) program at Sandia National Laboratories. Sandia National Laboratories is a multi-program laboratory managed and operated by Sandia Corporation, a wholly owned subsidiary of Lockheed Martin Corporation, for the U.S. Department of Energy's National Nuclear Security Administration under contract DE-AC04-94AL85000. This work was improved by the comments of three anonymous reviewers.

## References

[1] D. S. Oliver, Y. Chen, Recent progress on reservoir history matching: A review, Computational Geosciences 15 (2011) 185–221.

[2] H. J. H. Franssen, A. Alcolea, M. Riva, M. Bakr, N. van der Wiel, F. Stauffer, A. Guadagnini, A comparison of seven methods for the inverse modelling of groundwater flow. Application to the characterization of well catchments, Advances in Water Resources 32 (2009) 851–872.

[3] H. Lee, D. Higdon, Z. Bi, M. Ferreira, M. West, Markov random field models of high-dimensional parameters in simulations of fluid flow in porous media, Technometrics 44 (3) (2002) 230–241.

[4] J. Wang, N. Zabaras, A Markov random field model of contamination source identification in porous media flow, International Journal of Heat and Mass Transfer 49 (2006) 939–950.

[5] J. Fu, J. J. Gómez-Hernández, A blocking Markov chain Monte Carlo method for inverse stochastic hydrogeological modeling, Mathematical Geosciences 41 (2009) 105–128.

[6] J. Fu, J. J. Gómez-Hernández, Uncertainty assessment and data worth in groundwater flow and mass transport modeling using a blocking Markov chain Monte Carlo method, Journal of Hydrology 364 (2009) 328–341.

[7] W. Li, O. A. Cirpka, Efficient geostatistical inverse methods for structured and unstructured grids, Water Resources Research 42, w06402. doi:10.1029/2005WR004668.

[8] L. Biegler, G. Biros, O. Ghattas, M. Heinkenschloss, D. Keyes, B. Mallick, Y. Marzouk, L. Tenorio, B. van Bloemen Waanders, K. Willcox (Eds.), Large-Scale Inverse Problems and Quantification of Uncertainty, John Wiley and Sons, Ltd, 2010.

[9] Y. M. Marzouk, H. N. Najm, Dimensionality reduction and polynomial chaos acceleration of Bayesian inference in inverse problems, Journal of Computational Physics 228 (6) (2009) 1862 – 1902. doi:DOI: 10.1016/j.jcp.2008.11.024.

[10] B. Jafarpour, D. McLaughlin, Efficient permeability parameterization with discrete cosine transform, in: The Proceedings of the SPE Reservoir Simulation Symposium, no. Paper SPE 106453, 2007.

[11] B. Jafarpour, D. B. McLaughlin, History matching with an ensemble Kalman filter and discrete cosine parameterization, Computational Geosciences 12 (2008) 227–244.

[12] B. Jafarpour, V. K. Goyal, D. B. McLaughlin, W. T. Freeman, Compressed history matching: Exploiting transform-domain sparsity for regularization of nonlinear dynamic data integration problems, Mathematical Geosciences 42 (2010) 1–27.

[13] M. A. R. Ferreira, Z. Bi, M. West, H. K. H. Lee, D. Higdon, Multi-scale modeling of 1-D permeability fields, in: J. M. Bernardo, M. J. Bayarri, J. O. Berger, A. P. Dawid, D. Heckerman, A. F. M. Smith, M. West (Eds.), Bayesian Statistics, Vol. 7, Oxford University Press, 2003, pp. 519–527.

[14] S. I. Aanonsen, D. Eydinov, A multiscale method for distributed parameter estimation with application to reservoir history matching, Computational Geosciences 10 (2006) 97–117.

[15] D. Higdon, H. Lee, Z. Bi, A Bayesian approach to characterizing uncertainty in inverse problems using coarse and fine scale information, IEEE Transactions in Signal Processing 50 (2) (2002) 389–399.

[16] Y. Efendiev, T. Hou, W. Luo, Preconditioning Markov chain Monte Carlo simulations using coarse-scale models, SIAM Journal for Scientific Computing 28 (2) (2006) 776–803.

[17] Y. Efendiev, T. Hou, Multiscale finite element methods for porous media flows and their applications, Applied Numerical Mathematics 57 (5-7) (2007) 577–596, special Issue for the International Conference on Scientific Computing. doi:DOI: 10.1016/j.apnum.2006.07.009.

[18] J. A. Christen, C. Fox, Markov chain Monte Carlo using an approximation, Journal of Computational and Graphical Statistics 14 (4) (2005) 795–810.

[19] M. Hayek, F. Lehmann, P. Ackerer, Adaptive multi-scale parameterization for one-dimensional flow in unsaturated porous media, Advances in Water Resources 31 (2008) 28–43.

[20] I. Berre, M. Lien, T. Mannseth, A level-set corrector to an adaptive multiscale permeability prediction, Computational Geosciences 11 (2007) 27–42.

[21] L. K. Nielsen, H. Li, X.-C. Tai, S. I. Aanonsen, M. Espedal, Reservoir description using a binary level set method, Computing and Visualization in Science 13 (2010) 41–58.

[22] I. Berre, M. Lien, T. Mannseth, Multilevel parameter structure identification for two-phase porous-media flow problems using flexible representations, Advances in Water Resources 32 (2009) 1777–1788.

[23] M. Sahimi, Flow and transport in porous media and fractured rock: From classical methods to modern approaches, Wiley-VCH, 1995.

[24] K. S. Mendelsohn, A theorem on the effective conductivity of a two-dimensional heterogeneous medium, Journal of Applied Physics 46 (11) (1975) 4740–4741.

[25] A. H. Sihvola, J. A. Kong, Effective permittivity of dielectric mixtures, IEEE Transactions on Geosciences and Remote Sensing 26 (4) (1988) 420–429.

[26] G. Dagan, Models of groundwater flow in statistically homogeneous porous formations, Water Resources Research 15 (1) (1979) 47–63.

[27] G. Dagan, Flow and transport in porous media, Springer-Verlag, 1989.

[28] A. D. Poley, Effective permeability and dispersion in locally heterogeneous aquifers, Water Resources Research 24 (11) (1988) 1921–1926.

[29] S. Pozdniakov, C. F. Tsang, A self-consistent approach for calculating the effective hydraulic conductivity of a binary, heterogeneous medium, Water Resources Research 40, doi:10.1029/2003WR002617. W05105.

[30] T. Miloh, Y. Benveniste, A generalized self-consistent method for the effective conductivity of composites with ellipsoidal inclusions and cracked bodies, Journal of Applied Physics 63 (3) (1988) 789–796.

[31] T. Miloh, Y. Benveniste, On the effective conductivity of composites with ellipsoidal inhomogeneities and highly conducting interfaces, Proceedings of the Royal Society of London, A 455 (1999) 2687–2706.

[32] R. W. Zimmerman, Effective conductivity of a two-dimensional medium containing elliptical inhomogeneities, Proceedings of the Royal Society (452) (1996) A1713–A1727.

[33] P. Renard, G. de Marsily, Calculating equivalent permeability: A review, Advances in Water Resources 20 (5-6) (1997) 253–78.

[34] C. Knudby, J. Carrera, J. D. Bumgardner, G. E. Fogg, Binary upscaling: The role of connectivity and a new formula, Advances in Water Resources 29 (2006) 590–604.

[35] A. J. Desbarats, Numerical estimation of effective permeability in sand-shale formations, Water Resources Research 23 (2) (1987) 273–286.

[36] A. R. Solow, Mapping by simple indicator kriging, Mathematical Geology 18 (3) (1986) 335–352.

[37] A. G. Journel, F. Alaber, Non-Gaussian data expansion in the earth sciences, Terra Nova 1 (2) (1989) 123–134.

[38] J. J. Gómez-Hernández, R. M. Srivastava, ISIM3D: An ANSI-C three-dimensional multiple indicator conditional simulation program, Computers and Geosciences 16 (4) (1990) 395–440.

[39] GSLIB: Geostatistical Software Library and User's Guide, Oxford University Press, 1998.

[40] S. F. Carle, G. E. Fogg, Transition probability-based indicator geostatistics, Mathematical Geology 28 (4) (1996) 453–476.

[41] S. F. Carle, G. E. Fogg, Modeling spatial variability with one and multidimensional continuous lag markov chains, Mathematical Geology 29 (7) (1997) 891–918.

[42] C. Lantuejoul, Geostatistical Simulation: Models and Algorithms, Springer-Verlag, 2002.

[43] M. Armstrong, A. G. Galli, H. Beucher, G. Loch, D. Renard, B. Doligez, R. Eschard, F. Geffroy, Plurigaussian Simulations in Geosciences, Springer, 2003.

[44] R. J. Adler, On excursion sets, tube formulas and maxima of random fields, Annals of Applied Probability 10 (1) (2000) 1–74.

[45] R. J. Adler, J. E. Taylor, K. J. Worsley, Applications of Random Fields and Geometry: Foundations and Case Studies, 2009.

[46] J. E. Taylor, R. J. Adler, Euler characteristics for Gaussian fields on manifolds, The Annals of Probability 31 (2) (2003) 533–563.

[47] K. J. Friston, K. J. Worsley, R. S. J. Frackowiak, J. C. Mazziotta, A. C. Evan, Assessing the significance of focal activations using their spatial extent, Human Brain Mapping 1 (1994) 210–220.

[48] K. J. Worsley, S. Marrett, P. Neelan, A. C. Evans, Searching scale space for activation in PET images, Human Brain Mapping 4 (1) (1996) 74–90.

[49] D. J. Nott, R. J. Wilson, Multi-phase image modelling with excursion sets, Signal Processing 80 (2000) 125–139.

[50] F. M. Phillips, J. L. Wilson, An approach to estimating hydraulic conductivity spatial correlation scales using geological characteristics, Water Resources Research 25 (1) (1989) 141–143.

[51] S. A. McKenna, J. Ray, Y. Marzouk, B. van Bloemen Waanders, Truncated multiGaussian fields and effective conductance of binary media, Advances in Water Resources 34 (2011) 617–626.

[52] W. R. Gilks, S. Richardson, D. J. Spiegelhalter (Eds.), Markov Chain Monte Carlo in Practice, Chapman & Hall, 1996.

[53] H. Haario, E. Saksman, J. Tamminen, An adaptive Metropolis algorithm, Bernoulli 7 (2001) 223–242.

[54] H. Haario, M. Laine, A. Mira, E. Saksman, DRAM-Efficient adaptive MCMC, Statistics and Computing 16 (4) (2006) 339–354.

[55] J. Goodman, A. D. Sokal, Multigrid Monte-Carlo method: conceptual foundations, Physical Review D 40 (1989) 2035–2071.

[56] H. Haario, E. Saksman, J. Tamminen, Adaptive proposal distribution for random-walk Metropolis algorithm, Computational Statistics 14 (1999) 375–395.

[57] L. Tierney, A. Mira, Some adaptive Monte Carlo techniques for Bayesian inference, Statistics in Medicine 18 (1999) 2507–2515.

[58] P. J. Green, A. Mira, Delayed rejection in reversible jump Metropolis-Hastings, Biometrika 88 (2001) 1035–1053.

[59] A. Mira, Ordering and improving the performance of Monte Carlo Markov Chains, Statistical Science 16 (2002) 340–350.

[60] J. E. Aarnes, T. Gimse, K.-A. Lie, Geometric modelling, numerical simulation, and optimization, Springer, 2007, Ch. An introduction to the numerics of flow in porous media using Matlab, pp. 265–306. doi:10.1007/978-3-540-68783-2_9.

[61] J. Bell, P. Colella, A second-order projection method for the incompressible Navier-Stokes equations, J. Comp. Phys. 85 (1989) 257–283.

[62] R. J. Adler, J. E. Taylor, Random fields and geometry, Springer, 2007.

[63] M. Griogoriu, Stochastic calculus, Birkhauser, 2002.

[64] K. Schulgasser, On the conductivity of fiber reinforced materials, Journal of Mathematical Physics 17 (1976) 382–387.

[65] A. W. Harbaugh, MODFLOW-2005, the U.S.Geological Survey modular groundwater model – the ground water flow process, U.S. Geological Survey Techniques and Methods 6-A16, U.S. Geological Survey (2005).

[66] D. W. Pollack, User's guide for MODPATH/MODPATH-PLOT, Version 3: A particle tracking post-processing package for modflow, the U.S. Geological Survey finite-difference ground-water flow model, U.S. Geological Survey Open-File Report 94-464, U.S. Geological Survey (1994).

[67] A. E. Raftery, S. M. Lewis, The number of iterations, convergence diagnostics and generic metropolis algorithms, in: W. R. Gilks, D. J. Spiegelhalter, S. Richardson (Eds.), Practical Markov Chain Monte Carlo, Chapman and Hall, 1995.

[68] G. R. Warnes, mcgibbsit: Warnes and Raftery's MCGibbsit MCMC diagnostic, R package version 1.0.5 (2005).

[69] R Development Core Team, R: A Language and Environment for Statistical Computing, R Foundation for Statistical Computing, Vienna, Austria, ISBN 3-900051-07-0 (2008).

[70] J. Ray, S. A. McKenna, B. van BloemenWaanders, Y. M. Marzouk, Bayesian estimation of unresolved fine-scale properties of binary media from multi-scale observations, SAND Report SAND2011-3079, Sandia National Laboratories, Livermore, CA 94550-0969, unclassified unlimited release; available at http://csmr.ca.sandia.gov/∼jairay/index.html (May 2011).

[71] T. Gneiting, A. E. Raftery, Strictly proper scoring rules, prediction, and estimation, Journal of the American Statistical Association 102 (477) (2007) 359–378. arXiv:http://pubs.amstat.org/doi/pdf/10.1198/016214506000001437, doi:10.1198/016214506000001437.
URL http://pubs.amstat.org/doi/abs/10.1198/016214506000001437

[72] T. Gneiting, F. Balabdaoui, A. E. Raftery, Probabilistic forecasts, calibration and sharpness, Journal of the Royal Statistical Society: Series B (Statistical Methodology) 69 (2) (2007) 243–268. doi:10.1111/j.1467-9868.2007.00587.x.
URL http://dx.doi.org/10.1111/j.1467-9868.2007.00587.x

[73] J. Ray, S. Lefantzi, K. Klise, S. A. McKenna, B. van BloemenWaanders, M. D. Parno, Y. M. Marzouk, Bayesian data assimilation for stochastic multiscale models of transport in porous media, SAND Report SAND2011-6811, Sandia National Laboratories, Livermore, CA 94550-0969, unclassified unlimited release; available at http://csmr.ca.sandia.gov/∼jairay/index.html (October 2011).